Cal Poly

Caltech

SCEC
AN NSF+USGS CENTER

UC Irvine

UCLA

UC Santa Barbara

USC

Site Characterization and Liquefaction Analysis at Searles Lake, CA following 2019 Ridgecrest Earthquake Sequence

Timothy M. O'Donnell, Kenneth S. Hudson, Francisco Javier G. Ornelas, Jonathan P. Stewart, and Scott J. Brandenberg
Civil and Environmental Engineering
UCLA, Los Angeles, CA

Chukwuebuka C. Nweke
Civil & Environmental Engineering
University of Southern California

Paolo Zimmaro
Environmental Engineering
University of Calabria, Arcavacata di Rende, Italy

A report on research conducted with support of USGS

Report GIRS-2024-03

DOI: 10.34948/N3F302

University of California, Los Angeles (headquarters)

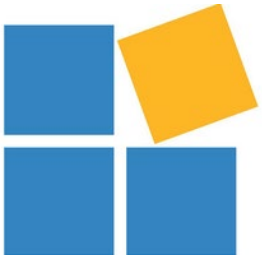

Natural Hazards Risk & Resiliency Research Center

B. John Garrick Institute for the Risk Sciences

Site Characterization and Liquefaction Analysis at Searles Lake, CA following 2019 Ridgecrest Earthquake Sequence

Timothy M. O'Donnell
Kenneth S. Hudson, Ph.D.
Francisco Javier G. Ornelas
Jonathan P. Stewart, Ph.D., P.E.
Scott J. Brandenberg, Ph.D., P.E.
Civil and Environmental Engineering
UCLA, Los Angeles, CA

Chukwuebuka C. Nweke, Ph.D.
Dept. of Civil and Environmental Engineering
University of Southern California, Los Angeles, CA

Paolo Zimmaro, Ph.D.
Dept. of Environmental Engineering
University of Calabria, Arcavacata di Rende, Italy

A report on research conducted with support from the USGS

Report GIRS-2024-03
DOI: 10.34948/N3F302

Natural Hazards Risk and Resiliency Research Center
B. John Garrick Institute for the Risk Sciences
University of California, Los Angeles (Headquarters)

March 2024

ABSTRACT

Following and during the 2019 Ridgecrest Earthquake Sequence (July 4 **M**6.5 event and July 5 **M**7.1 event), the Geotechnical Extreme Events Reconnaissance (GEER) Association conducted reconnaissance in areas with extensive surface manifestation of liquefaction at Searles Lake, near Trona and Argus, CA (GEER 2019, Zimmaro et al. 2020). Searles Lake is an ancient endorheic lakebed currently used as a mineral mine by Searles Valley Minerals (SVM). The reconnaissance documented broad regions that had experienced surface manifestation of liquefaction and other regions with no ground failure. As such, this site was considered an ideal case history for investigations of the factors leading to surface manifestation of liquefaction or the lack thereof.

After site access was secured from SVM, a site investigation was undertaken that began with field reconnaissance aimed at identifying specific locations for subsurface characterization and evaluation of the appropriate testing equipment. The surficial lakebed soils were deemed too soft for heavy equipment, so the investigation was planned as cone penetration test (CPT) soundings by Gregg Drilling LLC through road embankments and hand augers with tube sampling on adjacent lakebed areas. The subsurface investigation was carried out on May 22-23, 2023 in proximate locations with and without surface manifestation of liquefaction. The investigation consisted of five CPT soundings, two of which were seismic CPTs that included downhole shear wave velocity testing. The CPT depths were limited to approximately 10 m because of concerns of penetrating a confined aquifer at a depth of roughly 15 m. Four hand augered borings were advanced by the UCLA team to sample soil layers of interest identified from the CPT logs; borehole depths ranged from 2.2 to 4.0 m beneath the lakebed surface.

Site conditions were found to consist of a surficial lacustrine overconsolidated clay that extends to 3-4 m depth (below roadway) and overlies a silty sand layer with a soil behavior type index, I_C, < 2.6. The silty sand material was found to have a darkish, black hue, consistent with the color of observed sand boil materials from the post-earthquake reconnaissance, suggesting this layer produced the surface ejecta.

Tube samples of the surficial clay materials and dark silty sand were retrieved for testing at the UCLA soil dynamics laboratory. Laboratory testing consisting of specific gravity, bulk density, grain size distribution, and Atterberg Limits were conducted on samples of the silty sand materials and clay layers. Additionally, velocity time series retrieved from the downhole geophones used in seismic CPTs were interpreted to develop travel time picks and a shear wave velocity profile, from which a time-average shear wave velocity for the upper 30 m of the site (V_{S30}) was estimated as 175 m/s.

Analyses conducted for this case history included ground motion estimation, analyses of layer susceptibility and triggering, and analyses of surface manifestation of liquefaction for comparison to the field observations.

Because there were no ground motion recordings from the 2019 Ridgecrest Earthquake sequence in the immediate vicinity of the site, ground motion intensity measures were estimated from regional recordings using an approach that spatially interpolates within-event residuals (Pretell et al. 2024). That approach accounts for local site response using the site V_{S30} with an ergodic model. The ground motion interpolation approach was implemented in the python program, gmKriger, which estimated median-component Peak Ground Accelerations (PGAs) from the July 4 and July 5 events of 0.234g and 0.28g, respectively with natural log standard deviations of 0.509 and 0.477, respectively. The PGA of the larger July 5 event was considered the critical PGA and thus was used for all liquefaction analyses.

The site profile, including soil properties from the CPT soundings, were combined with the site PGA to perform liquefaction analyses. We considered two models. First, we applied a CPT-based model from Boulanger and Idriss (2016) that is commonly understood to be a liquefaction triggering model, but which in effect predicts surface manifestation based on analysis of a critical layer. Second, we considered the probability of surface manifestation of liquefaction model developed by the Next Generation Liquefaction (NGL) modeling team (Hudson et al. 2024). The NGL model is distinct in that it considers probabilities of liquefaction susceptibility and triggering on a layer-by-layer basis, then uses that information with various profile attributes to estimate the probabilities of liquefaction surface manifestation for the profile. Taking the silty sand layer as the critical layer, the Boulanger and Idriss model assigns a probability of liquefaction manifestation of well over 85% for all CPT soundings, including those for which manifestation was and was not observed (i.e., true positives and false positives, respectively). The NGL model assigns probabilities of liquefaction manifestation of 0.48-0.58 (median of 0.52) to the CPTs within the surface manifestation of liquefaction zone and 0.47 to the one CPT outside of the surface manifestation of liquefaction zone.

The data from this case history has been uploaded to the NGL database (Ulmer et al. 2022) for use by liquefaction researchers and will soon be published to DesignSafe.

Keywords: Surface Manifestation of Liquefaction, 2019 Ridgecrest Earthquake Sequence, Next Generation Probabilistic Liquefaction Manifestation Model

ACKNOWLEDGMENTS

This research was funded by the United States Geological Survey. We would like to thank Steven Kourakos of Searles Valley Minerals for helping us coordinate the site investigation as well as Peter Robertson and Brian Savela of Gregg Drilling LLC for facilitating the CPT testing for this project. We would also like to thank Dr. Renmin Pretell of the University of Nevada, Reno for helping us with the use of gmKriger.

CONTENTS

LIST OF TABLES

LIST OF FIGURES

1 INTRODUCTION

1.1 DEFINITION OF TERMS

In this report, we present a *case history* of ground performance involving surface manifestations and non-ground failure in proximate areas within an ancient endorheic lakebed from the 2019 Ridgecrest Earthquake sequence. In this context, a case history has three major elements (Stewart et al. 2016): (1) it involves a specific location, or a series of locations, where observations of ground performance were made and documented after an earthquake; (2) it includes the results of site characterization that identifies site stratigraphy and the engineering properties of relevant soil layers; and (3) it provides a measurement or estimate of the severity of ground shaking at the site location along with information about the causative earthquake event.

The ground failure mechanisms investigated through these case histories are related to liquefaction, which is generally defined as severe strength loss in saturated granular soils due to undrained (generally cyclic) shearing. In the presentation of the case histories, we will use terminology related to distinct issues that should be considered in the analysis of liquefaction problems. This section defines those terms. The terminology is that developed for the Next Generation Liquefaction project modeling effort (Hudson et al. 2024).

Surface manifestation refers to evidence of liquefaction at the ground surface, generally in the form of sand boils, ground cracking, settlement, and other effects. *Non-ground failure* indicates that a specific observation was made that these effects were not present at a site following an earthquake. Surface manifestation or non-ground failure are attributes of a *soil profile*, which is a collection of *soil layers* with different characteristics and occurring at different depths.

An individual soil layer may be judged to be *susceptible* or not to potential liquefaction. Susceptibility is related to fundamental material characteristics of the soil that control the level of pore pressure generation and strength loss that is possible if the soil were to be cyclically sheared. Susceptibility is unrelated to the density and current saturation level of the soil; while both of these factors affect the potential for triggering, they do not control the fundamental behavior of a soil. Susceptible soils include both predominantly coarse-grained and fine-grained granular soils.

Liquefaction triggering occurs in liquefaction-susceptible soils when the soils are saturated (or nearly so) and the liquefaction demand exceeds the soil's capacity to resist liquefaction. Triggering is a consequence of pore pressure generation in the soil, which leads to strength loss. However, that strength loss can be temporary and disappear upon further shearing of the soil, or may persist for longer periods of time, depending on profile and soil density characteristics.

The NGL models for liquefaction effects consider, during an interim step, probabilities of susceptibility and triggering for individual soil layers in a profile. Based on those results, along with other layer characteristics that may include penetration resistance, depth range, and information related to soil type, an assessment of layer and profile manifestation is conducted based on inferences from case history data. Model performance is assessed by comparing profile manifestation predictions to observations from sites subjected to strong shaking from earthquakes. This report documents a case history and assesses model performance in this manner.

1.2 MOTIVATION AND SCOPE

The motivation for this project was to develop and analyze case histories for sites within Searles Lake CA for which post-earthquake observations of field performance was performed shortly following the 2019 Ridgecrest Earthquake Sequence. These sites were of special interest because they all experienced similar levels of shaking and have similar site geology, but different levels of ground performance (surface manifestation and lack thereof) occurred. As a result, the sites were anticipated to be especially valuable for identifying factors related to individual profiles and soil layers that may lead to the different levels of performance. Development of the case histories required performing site characterization and estimating ground motions.

Site characterization began by developing a site investigation plan and coordinating with members of Searles Valley Minerals (SVM), who own the site, and Gregg Drilling LLC, who performed the Cone Penetration Testing (CPT) equipment, to execute that plan. After the investigation, a laboratory testing program was carried out at UCLA on select samples to better characterize the soil layers that were sampled from hand-augered boreholes. Significantly, samples of black silty sand, resembling the sand boil ejecta that was documented immediately after the 2019 Ridgecrest Earthquake Sequence, were recovered at various depths from all of the hand augered borings. Laboratory testing was carried out on these samples to obtain parameters that are often used for liquefaction analysis (like gradation and plasticity) and to assign a USCS Classification. Results of the site characterization are described in Chapter 3 of this report.

The case histories developed in this project were not considered in either the training or testing datasets employed during the development of the NGL models (Hudson 2023; Hudson et al. 2024), which separately consider susceptibility, triggering, and manifestation as defined in Section 1.1. As such, these case histories provide an independent basis from which to assess performance of the NGL model and legacy models. These analyses are documented in Chapter 4 of this report.

2 2019 RIDGECREST EARTHQUAKE SEQUENCE

2.1 SITE GEOLOGIC HISTORY

Searles Valley is located in a Basin and Range geomorphic province (i.e., an area characterized by the presence of abrupt changes in elevation, which alternate mountain chains with valleys and/or basins), near the Mojave Desert geomorphic province. This area contains multiple seismogenic faults including the roughly east-west trending Garlock fault to the south and the north-south trending Little Lake, Salt Wells Valley, and Paxton Ranch fault zones to the east. These fault zones are part of the Eastern California Shear Zone (ECSZ), which accommodates plate boundary deformation east of the San Andreas fault and extends from the southern Mojave Desert to the east side of the Sierra Nevada mountain range. The area comprises numerous interior drainage systems with lakes and playas and horst-and-graben geologic structure (subparallel, fault-bounded ranges separated by down-dropped basins) that include valleys such as Death Valley, Owens Valley, Honey Lake Basin, and associated mountain ranges (Frankel et al. 2008, Liu et al 2010).

Searles Valley is an alluvial basin characterized by alluvial fan deposits on the flanks of the surrounding mountains with lacustrine deposits in the interior of the basins. The alluvial deposits are derived from the surrounding mountains, which are primarily Paleozoic to late Mesozoic granitic bedrock (Kunkel and Chase, 1969) and volcanic deposits (Schweig, 1984).

Searles Valley has a stratigraphy comprising Pleistocene and Holocene alluvium, consisting of fine-to-coarse sand with little gravel and fines, Holocene playa silt and clay, and Holocene aeolian dune sand. However, the lacustrine deposits differ in that they contain thick evaporite deposits interbedded with lacustrine silts and clays. The evaporites consist primarily of halite, thermonatrite, thenardite, and ulexite with gypsum, locally common in some units (Smith, 2009). The valley includes the hydrographically-closed Searles Valley Groundwater Basin, which was once connected to other groundwater basins. The current lack of connection between basins in this area makes it drier than in the past (McGraw et al., 2016). The groundwater table in the central–western portion of the Searles Lake playa ranges from depths less than 1 to approximately 2 m (California DWR, 2020). The groundwater in this basin is a brine with pH values between 9.2 and 9.5 (Smith, 1979).

2.2 EARTHQUAKE SEQUENCE AND FIELD OBSERVATIONS

The 2019 Ridgecrest earthquake sequence occurred in July 2019. A **M**7.1 July 5 mainshock occurred on the Paxton Ranch fault zone and was preceded by a **M**6.4 foreshock on July 4 on the Salt Wells Valley fault zone (Figure 2.1). These events caused massive liquefaction in the areas of Trona, Argus, and the Searles lakebed (Brandenberg et al., 2019 and 2020; Zimmaro et al., 2020), and surface fault ruptures along the two causative faults (Ponti et al., 2019; DuRoss et al., 2020) (Figure 2.1).

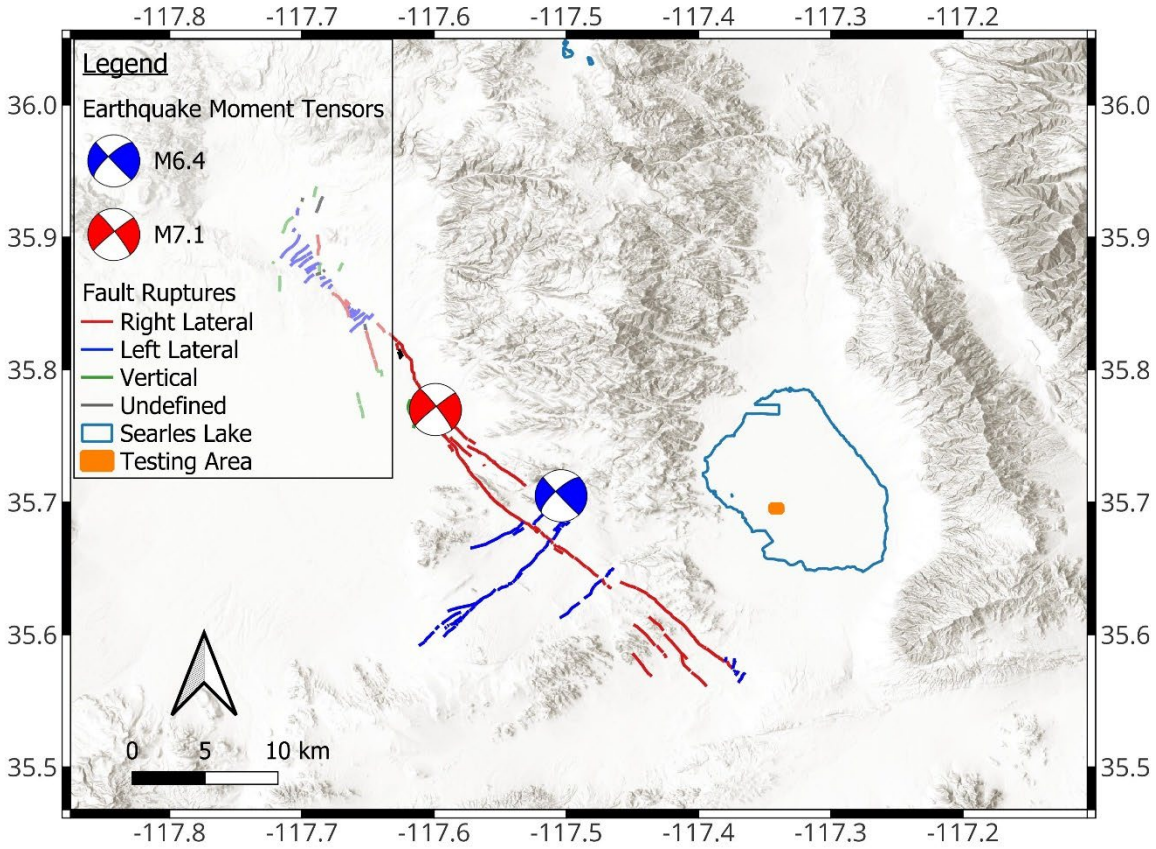

Figure 2.1. Overview of the 2019 Ridgecrest earthquake sequence area. Beachballs represent moment tensor solutions for the **M**6.4 and **M**7.1 events; color coded lines represent surface fault rupture features observed following the earthquake sequence.

Following the earthquake sequence, the Geotechnical Extreme Events Reconnaissance (GEER) Association conducted reconnaissance that included documentation of ground failure and non-ground failure in Searles Lake, near Trona and Argus, CA (Brandenberg et al., 2019; Zimmaro et al., 2020). Whereas manifestation in Trona and Argus, to the extent that it occurred, consisted mainly of tensile ground cracking that is difficult to associate with liquefaction, ground failure within the Searles Lake area was abundant and unambiguous regarding its relationship to liquefaction due to extensive boiling. Liquefaction surface manifestations were observed in large

portions of the lakebed, but areas without evidence of ground failure were also identified and mapped (Zimmaro and Hudson, 2019; Zimmaro et al., 2020). Most of these manifestations took the form of sand boils and ground cracks, with abundant sand ejecta. Brine ejecta manifestations, clearly caused by the earthquake sequence, were also present. Interestingly, most sand ejecta throughout the lakebed were characterized by a very dark, almost-black, color (Figures 2.2 and 2.3).

Figure 2.2. Satellite photo taken following the 2019 earthquake sequence of the South-West portion of the lake. Orange dots represent highlighted photo locations taken during the reconnaissance mission (Zimmaro and Hudson, 2019).

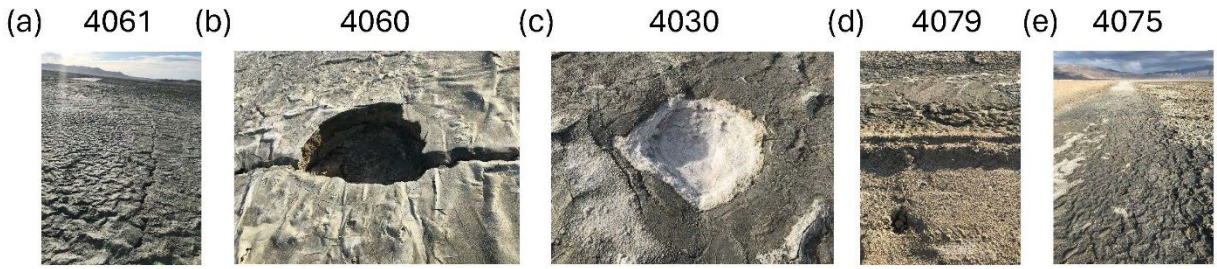

Figure 2.3. Selection of photos taken in the area shown in Figure 2.2: (a) Photo 4061 (massive liquefaction of dark-material ejecta), (b) Photo 4060 (sand boil), (c) Photo 4030 (sand boil with crystallized brine covering its surface), (d) Photo 4079 (narrow line of dark ejecta - photo taken from the top of the embankment where no liquefaction surface manifestation was observed), and (e) Photo 4075 (narrow elongated dark-ejecta feature).

This coloration of ejecta made it easier to identify layers responsible for these manifestations, which is discussed further in Chapter 3. While most liquefaction observations were made within the central portion of the lakebed, at the margins of the lake, patterns of ground failure in the form of relatively narrow (100-200 m-thick) concentric zones were also observed. One of the features making it a case study worthy of subsequent investigations is the fact that variable surface performances (i.e., liquefaction manifestations alternated with no surface manifestations within the same, narrow, area) were present at various locations. This aspect makes it an attractive area to perform separate liquefaction triggering and manifestation analyses and test legacy and newer analysis methods.

3 SITE CHARACTERIZATION

3.1 SITE INVESTIGATION PLAN

A site investigation plan was developed to characterize the subsurface of Searles Lake at areas of the lakebed where surface manifestations of liquefaction were documented by the reconnaissance team led by Zimmaro et al. (2020). A preliminary site visit was conducted by the UCLA team in September of 2022 to assess the feasibility of testing in the areas with the highest concentration of observed surface manifestations of liquefaction. It was found that the lakebed surface was too soft to support the weight of Gregg Drilling's truck mounted CPT rig (60,000 lb). Therefore, the spatial scope of the investigation was limited to areas where significant surface manifestation of liquefaction was observed near the access roadways. This led to the conclusion that the optimal spot to perform testing would be in an area where heavy surface manifestation of liquefaction was observed in the southern region of the lakebed, labeled "Testing Area" in Figure 3.1.

The plan originally consisted of six truck mounted CPT soundings to be performed by Gregg Drilling (SCPT-1, CPT-2, CPT-3, CPT-4, CPT-5, SCPT-6) and five hand augered borings to be dug by the UCLA team (HA-1, HA-1R, HA-2, HA-3, HA-4). Based on the observed field performance as presented in Section 2.3, SCPT-1, CPT-2, CPT-3, and CPT-4 as well as HA-1, HA-1R, HA-3, and HA-4 were considered to be in "surface manifestation of liquefaction" zones. Conversely CPT-5, CPT-6, and HA-2 were considered to be in "no surface manifestation of liquefaction" zones. One of the CPTs (CPT-5) encountered an obstruction and was therefore canceled. Because of the obstruction, SCPT-6 was moved a couple meters to the east and was thus renamed SCPT-6A. One of the borings (HA-2) was never started due to time constraints. At two of the CPT locations (SCPT-1 and SCPT-6), Seismic Cone Penetration Tests (SCPTs) were conducted for the purpose of measuring shear wave velocity. Finally, Horizontal-to-Vertical Spectral Ratio (HVSR) testing was conducted at various locations to estimate the resonant frequency of the site. The final site investigation plan that was executed on May 22 and Mat 23, 2023 is presented in Table 3-1 and Figure 3.1.

Table 3.1. Testing locations for site investigation plan.

Test Name	Test Type	Latitude	Longitude
SCPT-1	Seismic Cone Penetration Test	35.6939	-117.3386
CPT-2	Cone Penetration Test	35.6939	-117.3385
CPT-3	Cone Penetration Test	35.6939	-117.3384
CPT-4	Cone Penetration Test	35.6939	-117.3383
SCPT-6A	Seismic Cone Penetration Test	35.6939	-117.3381
HA-1R	Hand Augered Boring	35.6939	-117.3387
HA-1	Hand Augered Boring	35.6940	-117.3386
HA-3	Hand Augered Boring	35.6957	-117.3413
HA-4	Hand Augered Boring	35.6960	-117.3441
SV-1	Horizontal-to-Vertical Spectral Ratio	35.6942	-117.3388
SV-2	Horizontal-to-Vertical Spectral Ratio	35.6943	-117.3388
SV-3	Horizontal-to-Vertical Spectral Ratio	35.6958	-117.3411
SV-4	Horizontal-to-Vertical Spectral Ratio	35.6959	-117.3411
SV-1b	Horizontal-to-Vertical Spectral Ratio	35.6942	-117.3389
SV-2b	Horizontal-to-Vertical Spectral Ratio	35.6943	-117.3388
SV-5	Horizontal-to-Vertical Spectral Ratio	35.6956	-117.3412

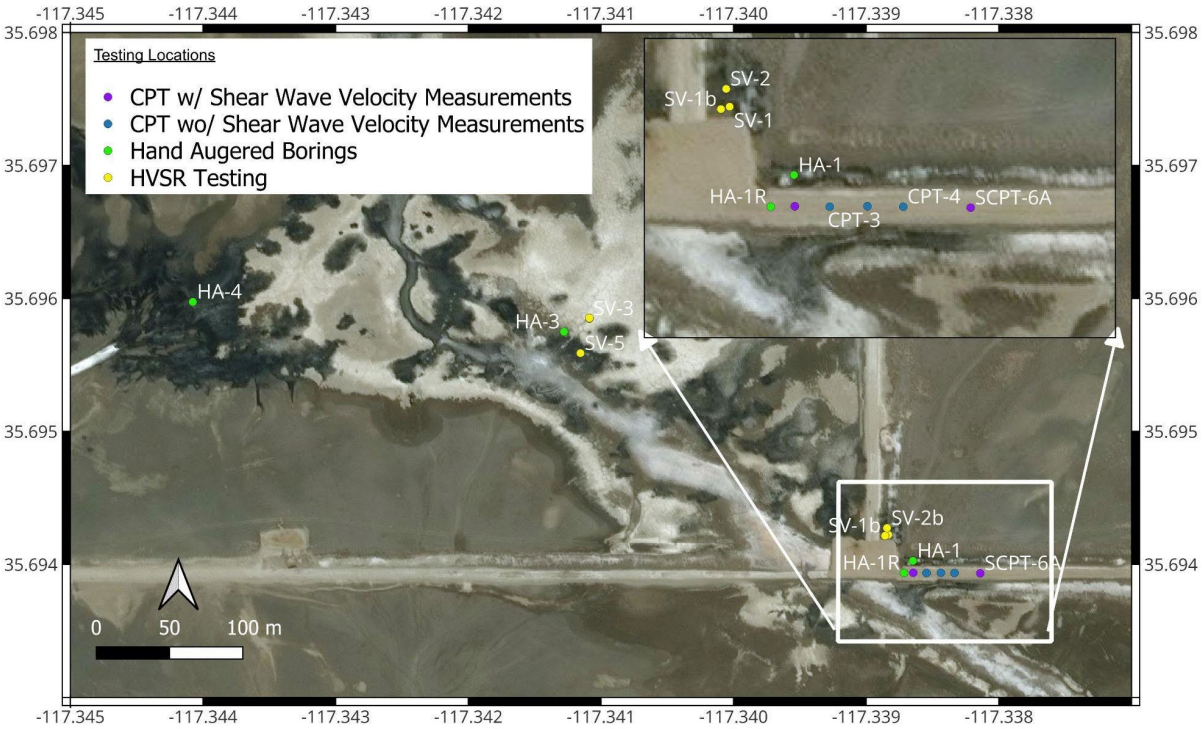

Figure 3.1. Testing locations for site investigation plan.

3.2 CONE PENETRATION TESTS

On May 22, 2023, Gregg Drilling LLC conducted five Cone Penetration Tests (CPTs) at the locations given in Table 3-1 and Figure 3.1. Figures 3.2 through 3.6 show results of the cone penetration tests SCPT-1, CPT-2, CPT-3, CPT-4, and SCPT-6A. Shear wave velocity measurements for the SCPT soundings are presented in the next section. All of the CPT soundings indicate the presence of a sandy fill layer overlying a predominantly clayey deposit with interbedded silty sand and sandy silt layers at depths between 3 and 4 m, and near 4.5 m. Values of soil behavior type index I_C (Robertson 1990) in the silty sand and sandy silt layers are between 1.5 and 2.6, and these layers are therefore considered susceptible to liquefaction.

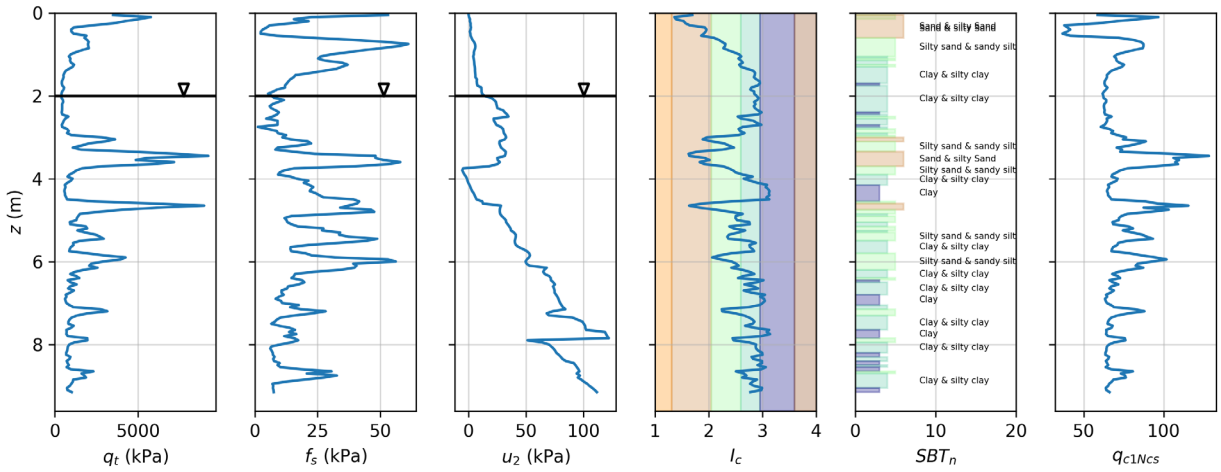

Figure 3.2. Cone penetration test results for SCPT-1.

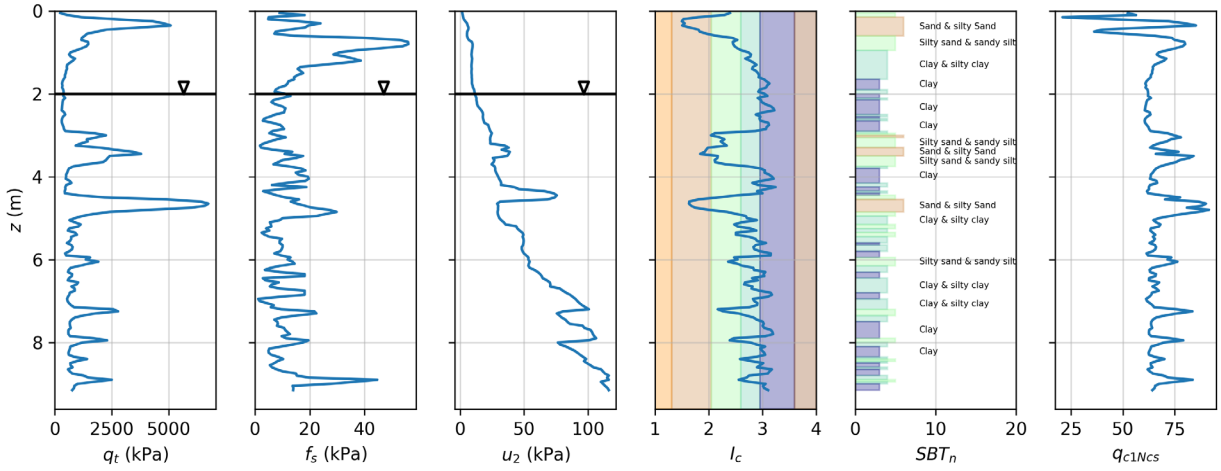

Figure 3.3. Cone penetration test results for CPT-2.

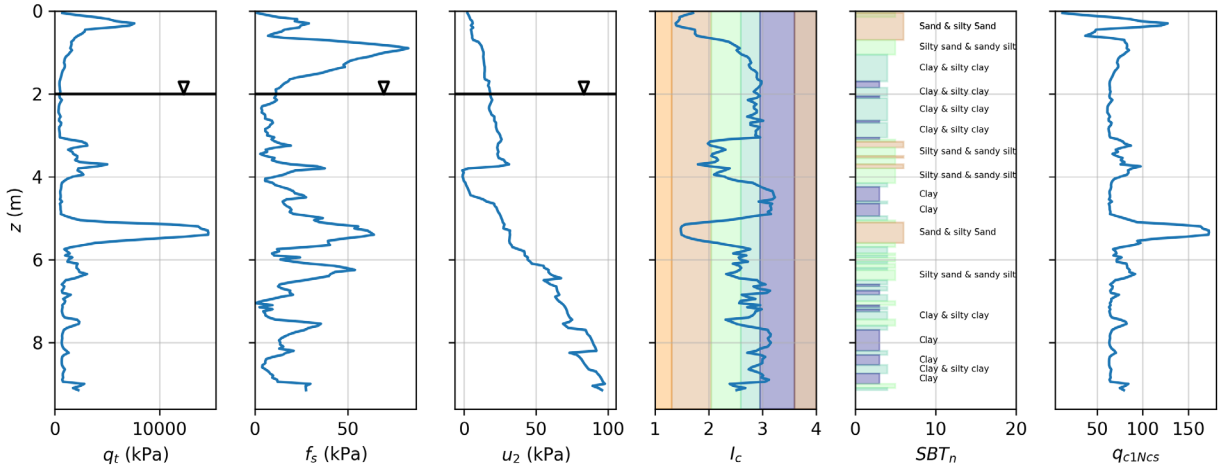

Figure 3.4. Cone penetration test results for CPT-3.

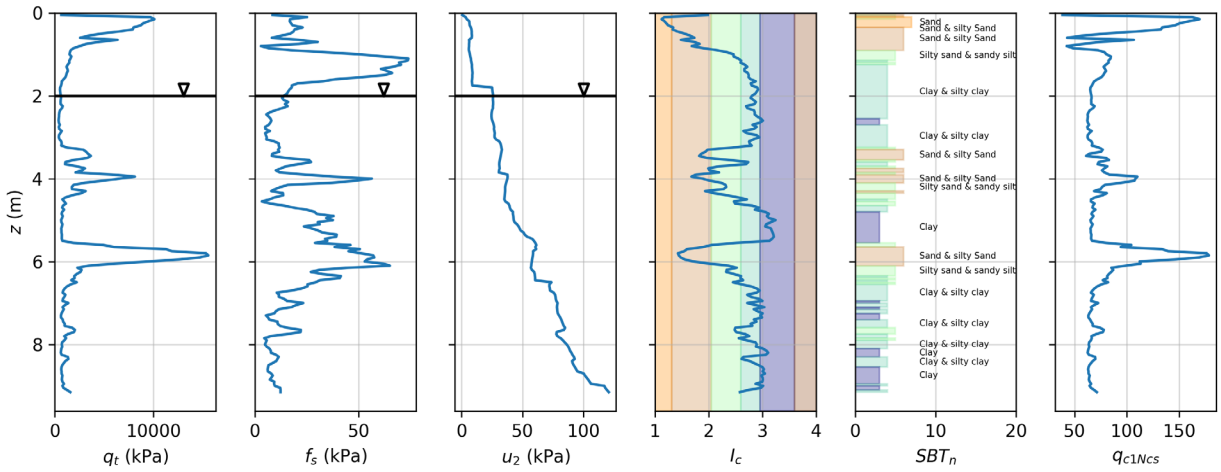

Figure 3.5. Cone penetration test results for CPT-4.

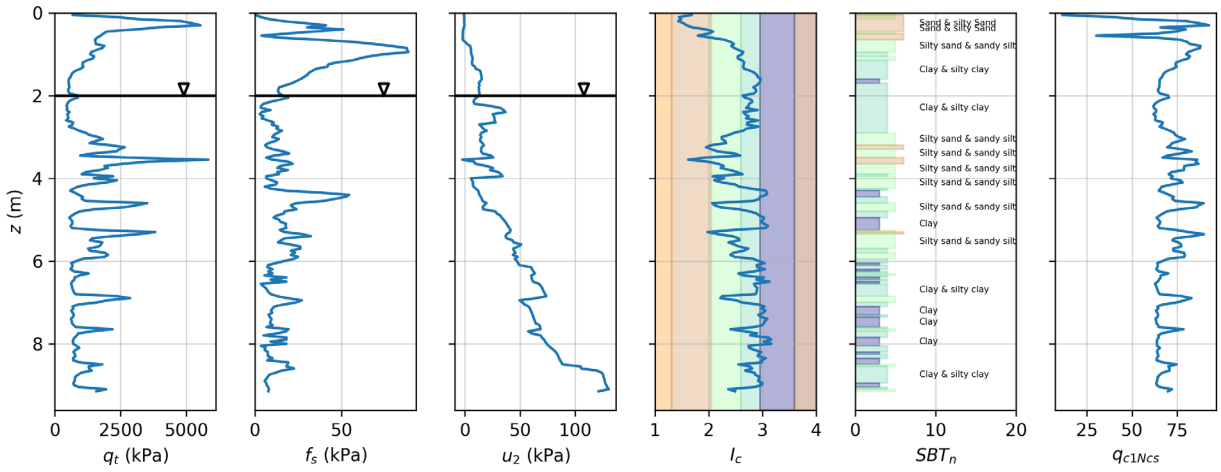

Figure 3.6. Cone penetration test results for CPT-6A.

3.3 SHEAR WAVE VELOCITY MEASUREMENTS

Down hole shear wave velocity measurements were made using seismic CPT soundings (SCPT) at SCPT-1 and SCPT-6A that were conducted by Gregg Drilling LLC on May 22, 2023. The automated travel time picks by Gregg Drilling (light blue points in Fig. 3.7) were not used. Rather, the raw geophone data was analyzed and consistent wave features (or "picks") were selected amongst the wave recordings at each depth interval for the purpose of calculating shear wave velocity. For both tests, no consistent wave features could be confidently identified at each depth interval. Therefore, for both tests, one feature was identified at depths of approximately 1.52, 3.05, and 4.75 m (5, 10, and 15 ft) and a different feature was identified at depths of 4.75, 6.10, 7.62, and 9.14 m (15, 20, 25, and 30 ft). The reason why a single feature did not persist in all geophone records is unclear, but may be related to the presence of the relatively stiff embankment overlying soft clay, and the reflections caused by the resulting impedance contrast.

For both SCPT-1 and SCPT-6A, pick 1 is selected at the location of the first peak of the signal represented by the red line and pick 2 is selected at the first prominent trough of the same feature. The raw geophone data and picks for SCPT-1 and SCPT-6A are shown in Figures 3.7 and 3.8, respectively.

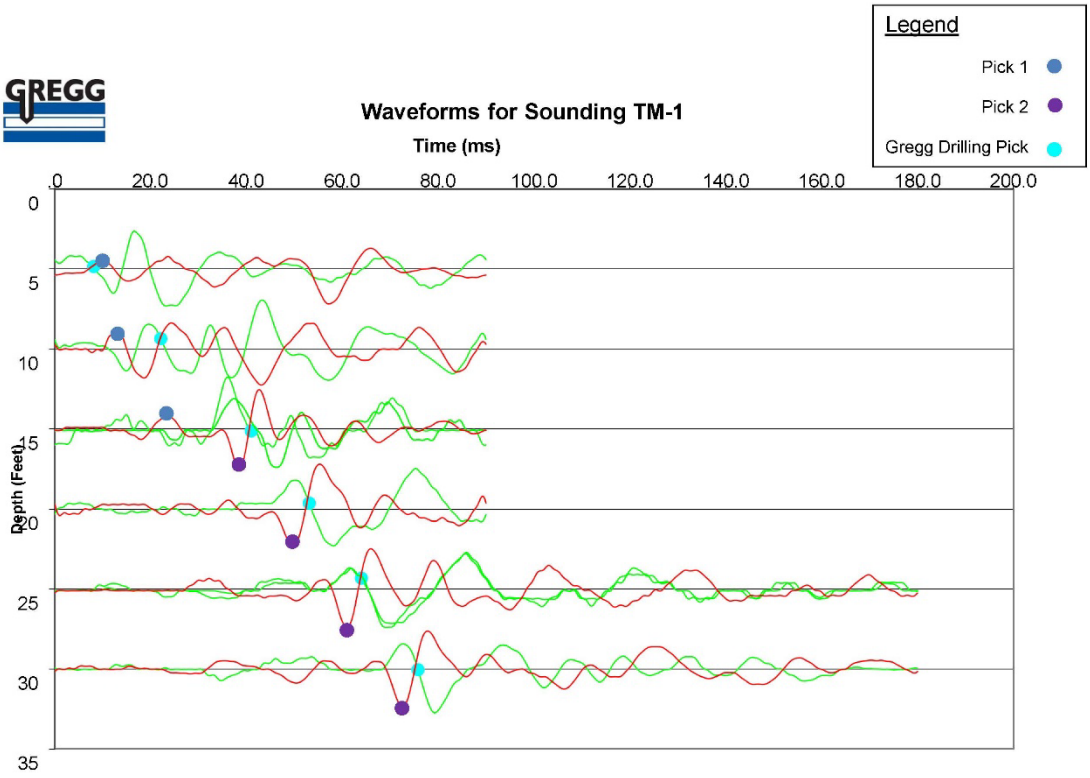

Figure 3.7. SCPT-1 raw geophone data with picks for shear wave velocity calculation.

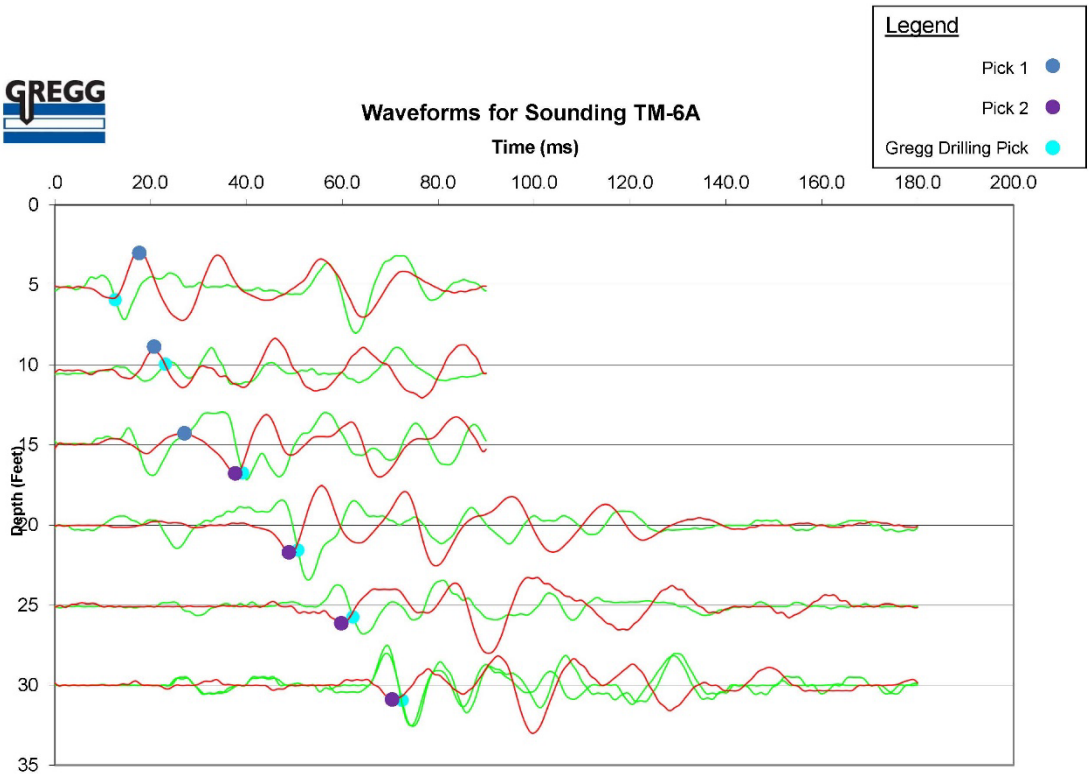

Figure 3.8. SCPT-6A raw geophone data with picks for shear wave velocity calculation.

For both SCPT-1 and SCPT-6A, the travel times corresponding to both picks were plotted against depth as shown in Figures 3.9 and 3.10. The gap in travel time of the two picks at a depth of approximately 15 ft. is plotted as Δtt.

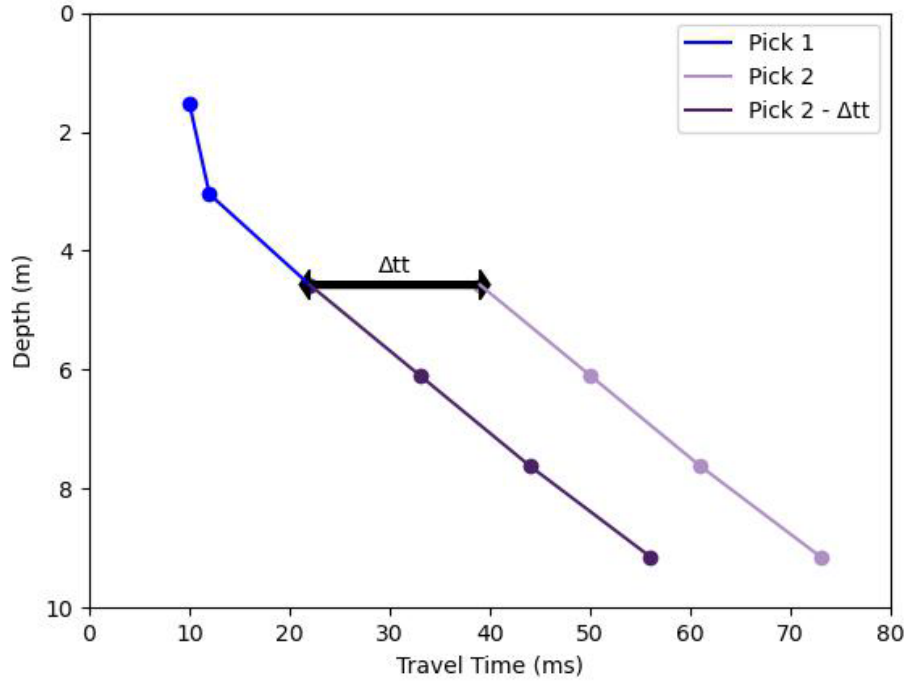

Figure 3.9. Travel time vs. depth for SCPT-1.

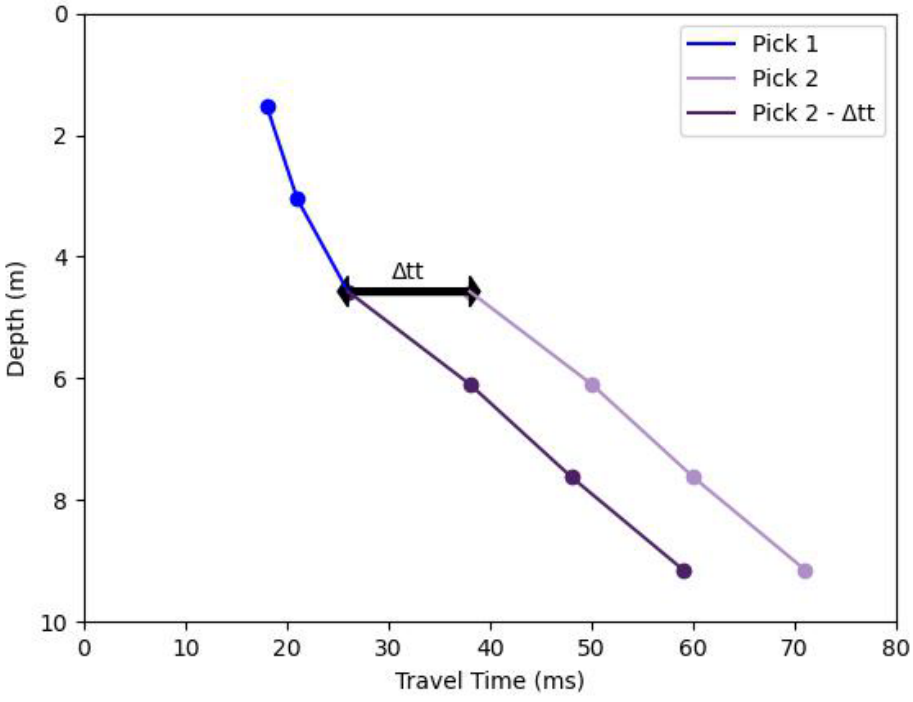

Figure 3.10. Travel time vs. depth for SCPT-6A.

For each depth interval, the shear wave velocity was calculated using Eq. 3.1, where Vs is shear wave velocity and tt is travel time in seconds.

$$Vs = \frac{Depth_{i+1} - Depth_i}{tt_{i+1} - tt_i} \quad (3.1)$$

Values of V_S computed for the deeper depth intervals were reasonable. However, a number of limitations are present in the V_S values computed at shallower depths. First, V_S is computed based on differences in travel time over a depth interval, as identified by the features corresponding to the different pick methods. These travel times should not be interpreted as the actual time required for the wave to travel from the surface to the specified depth because no single feature of the waveform is well-suited to directly measuring that travel time. For this reason, we cannot compute a travel time for the first interval from depth 0 to 1.52 m. Second, travel times computed for the depth interval from 1.52 to 3.05 m are 510 and 507 m/s for SCPT-1 and SCPT-6A, respectively, both of which are unreasonably high for the soft soils encountered at this site. This indicates that the SCPT results are unreliable at these depth intervals. For SCPT-6A, the peaks and troughs at a depth of 4.72 m (15 ft) do not correlate well with the peaks and troughs from the shallower measurements, and we therefore consider that interval to be unreliable.

To estimate V_S in the embankment fill from 0 to 1.37 m, we use correlations with CPT measurements proposed by Wair et al. (2012) and presented in the Ulmer et al. (2020) as indicated by Eqs. 3.2 through 3.4, where f_s is side friction in kPa, q_t is cone tip resistance in kPa, I_c is soil behavior index, z is depth in meters, σ_v is total overburden stress in kPa, and P_a is atmospheric pressure in kPa.

$$Vs = 118.8log(f_s) + 18.5 \quad (3.2)$$

$$Vs = 2.27(q_t)^{0.412}(I_c)^{0.989}(z)^{0.033} \quad (3.3)$$

$$Vs = \sqrt{\frac{10^{0.55I_c+1.68}(q_t-\sigma_v)}{P_a}} \quad (3.4)$$

Wair et al. suggests to take the average of the resulting three shear wave velocities calculated using the equations as the shear wave velocity estimate. Utilizing SCPT-1 to a depth of 1.37 m, the estimated shear wave velocity of the embankment fill using Wair's method was calculated to be 205 m/s. We consider this to be a reasonable value.

For the clay layer between the bottom of the embankment fill at a depth of 1.37 m to the top of the depth interval where we have reasonable velocity measurements at 3.05 m, we simply use the V_S measured for the 3.05 to 4.57 m depth interval. These values are summarized in Tables 3.2 and 3.3, and in Figures 3.11 and 3.12. The shear wave velocity decreases slightly with depth, which may be the result of fluctuations in the lakebed resulting in overconsolidation of the upper couple meters of the profile. This would cause the upper portion of the profile to have higher shear wave velocities, consistent with the shear wave velocity profile depicted in Figure 3.11.

Table 3.2. SCPT-1 shear wave velocity values.

$Depth_i$ (m)	$Depth_{i+1}$ (m)	tt_i (ms)	tt_{i+1} (ms)	Measured Vs (m/s)	Recommended V_S (m/s)
0	1.37	N/A	N/A	N/A	205[b]
1.37	1.52	N/A	N/A	N/A	154[c]
1.52	3.05	10	13	510[a]	154[c]
3.05	4.57	12	22	154	154
4.57	6.10	39	50	139	139
6.10	7.62	50	61	139	139
7.62	9.15	61	73	127	127
9.15	10.00	N/A	N/A	127	127[d]

[a] measured value considered unreasonable
[b] interpolated from cone tip resistance using Wair et al. (2012)
[c] extrapolated up from depth interval from 3.05 to 4.57 m
[d] extrapolated down from depth interval from 7.62 to 9.15 m

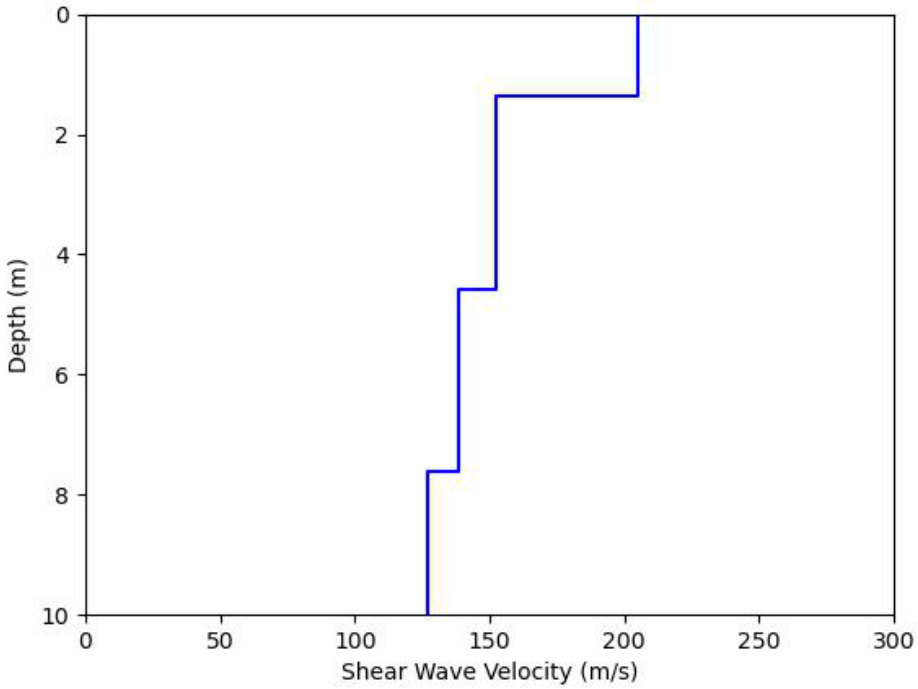

Figure 3.11. SCPT-1 shear wave velocity profile.

Table 3.3. SCPT-6A shear wave velocity values.

$Depth_i$ (m)	$Depth_{i+1}$ (m)	tt_i (ms)	tt_{i+1} (ms)	Measured V_S (m/s)	Recommended V_S (m/s)
0	1.37	N/A	N/A	N/A	205[b]
1.37	1.52	N/A	N/A	507[a]	127[c]
1.52	3.05	17	20	507[a]	127[c]
3.05	4.57	20	27	217[a]	127[c]
4.57	6.10	38	50	127	127
6.10	7.62	50	60	152	152
7.62	9.15	60	71	139	139
9.15	10.00	N/A	N/A	139	139[d]

[a] measured value considered unreasonable
[b] interpolated from cone tip resistance using Wair et al. (2012)
[c] extrapolated up from depth interval from 3.05 to 4.57 m
[d] extrapolated down from depth interval from 7.62 to 9.15 m

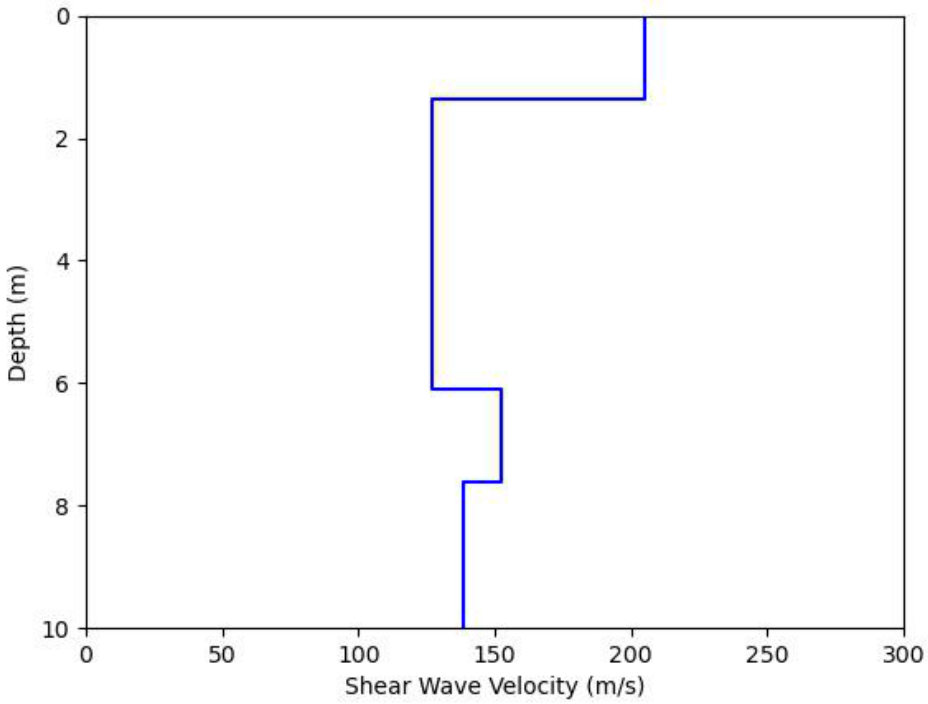

Figure 3.12. SCPT-6A shear wave velocity profile.

For the purpose of extrapolating the velocity profile to a depth of 30m, we extend the bottom of the profile to a depth of 10 m using the measured V_S for the deepest interval from 7.62 to 9.14 m. This is because we use the method of Dai et al. (2013) for extrapolating a velocity profile from Z to 30 m, where coefficients are specified for Z = 5, 10, 15, 20, and 25 m, so we therefore need a profile that extends to one of these depths. Using the shear wave velocity profiles, the travel time in the upper 10 m was computed using Eq. 3.5, where ΔH is the layer thickness (note that the layer thicknesses sum to 10m), and N_L is the number of layers. Values of tt_{10} were computed to be 0.068 s and 0.071 s for SCPT-1 and SCPT-6A, respectively.

$$tt_{10} = \sum_{i=1}^{N_L} \frac{\Delta H_i}{V_{S,i}} \tag{3.5}$$

To estimate the shear wave velocity of the upper 30 meters of the site (V_{S30}), first the formula proposed by Dai et al. (2013) to estimate the shear wave velocity from 10 to 30 meters was used, as defined by Eq. 3.6, where z = 10 meters in this case, V_{SZ30} is the time-averaged shear wave velocity from a depth of 10 to 30 meters, c_0 is model coefficient 1 which equals 0.642 in California, and c_1 is model coefficient 2 which equals 0.777 in California, and $V_S(z)$ is the shear wave velocity at a depth of 10 m (not to be confused with the time-averaged shear wave velocity in the upper 10 m), and is equal to 127 m/s for SCPT-1, and 139 m/s for SCPT-6A.

$$log(V_{SZ30}) = c_0 + c_1 log(V_s(z)) \tag{3.6}$$

Using Equation 3.6, the V_{SZ30} was found to be 189 m/s for SCPT-1 and 203 m/s for SCPT-6A. Finally, V_{S30} was computed using Eq. 3.7

$$V_{S30} = \frac{30}{tt_{10} + \frac{30-10}{V_{SZ30}}} \tag{3.7}$$

Using Equation 3.8, V_{S30} was estimated at SCPT-1 and SCPT-6A to be 172 and 177 m/s, respectively. We therefore used an average V_{S30} of 175 m/s for this site.

3.4 HORIZONTAL TO VERTICAL SPECTRAL RATIO TESTING (HVSR)

As part of the site characterization field work on May 22-23, 2023, seven microtremor horizontal-to-vertical spectral ratio (mHVSR) surveys were carried out in the Searles Valley lakebed (Ornelas et al. 2023). mHVSR is a technique that was initially proposed by Nogoshi and Igarashi (1971) and later popularized by Nakamura (1989). It is based on the principle that the microtremor horizontal wavefield is often amplified when seismic waves propagate through soil deposits compared to the vertical wavefield. Accordingly, peaks in mHVSR vs frequency plots can

illustrate resonant frequencies associated with impedance contrasts within the soil deposit. Studies have consistently shown that the lowest frequency peak found using mHVSR correlates to the fundamental frequency of the site (Lermo and Chavez-Garcia 1993; Lachet et al. 1996; Theodulidis et al. 1996). Measurements of mHVSR were performed as part of this study to provide information that could be useful in future work to refine ground motion estimates at the site from the 2019 Ridgecrest Earthquake Sequence. Figure 3.1 shows the locations at the site where these mHVSR surveys were performed.

The surveys were performed using a 3-component broadband temporarily deployed seismometers. The manufacturer of the seismometers is Nanometrics Inc., and the type of sensor used was a Trillium Compact Horizon 120s seismometer, which was attached to a Pegasus PGS-140 recorder. These seismometers have a flat frequency bandwidth from 0.0083 – 100 Hz (0.01 – 120 s). These tests were performed for a recording time of 2-3 hr with a sampling rate of 200 Hz. The sensors were partially buried 51-102 mm and covered with a 19-L bucket in order to increase the coupling of the sensor to the ground and to reduce any external noise such as wind. Moreover, some of these tests were performed using an electrical insulating blanket (referred to as E.M.F Blanket) in order to reduce the potential for electrical noise to distort the HVSR ordinates. Figure 3.13 shows the layout of the sensors with the blanket placed over the bucket.

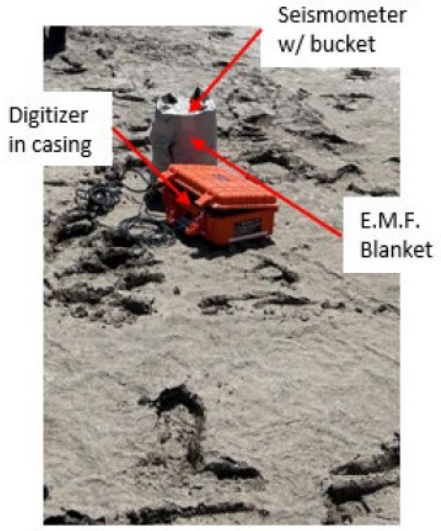

Figure 3.13. Layout of the seismometer and the digitizer used during testing in the Searles Valley Lakebed. In this image an EMF blanket was used to reduce the amount of electrical noise produced.

The data collected from these surveys was processed using processing procedures described in Wang et al. (2022), using the processing package *hvsrProc* (Wang 2021). Additionally, pre-processing steps were incorporated to reduce the amount of drift in the data which are described in Ornelas et al. (2024b). Figure 3.14 shows four mHVSR mean curves and standard deviation (in gray) of the tests performed in the lakebed. Figure 3.14 shows that two tests (a and b) performed in one area of the lakebed and another two tests (c and d) performed about 273 meters apart have

similar resonant frequencies (represented as peaks) across the lakebed for this area, which indicates the deep geology structure is relatively consistent.

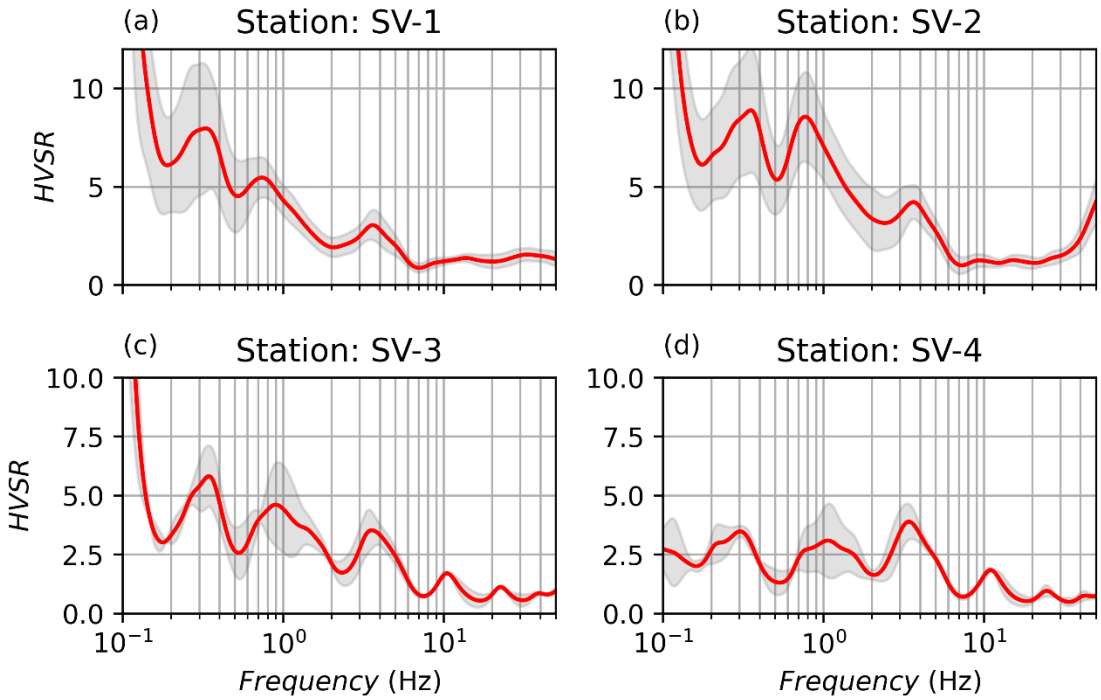

Figure 3.14. mHVSR spectra for four tests. (a) top left: Station SV-1, (b) top right: Station SV-2, (c) bottom left: Station SV-3, (d) bottom right: Station SV-4, each test showing the mean curve and standard deviation (in gray).

Three of the four test results have large values at low frequencies (< 0.15 Hz), which is a common problem with highly sensitive sensors used in temporary deployments as was done at this site (Ornelas et al. 2024b). Results at higher frequencies are more reliable, and consistently show first-mode resonances at 0.35 Hz and a higher mode resonance at about 0.8 Hz. It is likely that the 0.35 Hz resonance is associated with a deep velocity contrast, possibly related to the soil/rock contact, whereas the 0.8 Hz and higher resonance are likely associated with shallower horizons, possibly including the Holocene/Pleistocene boundary. The association of a peak with a particular horizon could only be confirmed with deep well log data, which was not available as part of this investigation.

Although not undertaken as part of this study, mHVSR spectra can be used to inform site response models. Prior work has shown promising results for localized regions with soft soils such as peat deposits (e.g., Wang et al. 2022a; Buckreis et al. 2024), although models generally applicable to broad geological conditions are not yet available. For this reason, there is merit in the collection of this mHVSR for potential future model development in the Ridgecrest and Searles Valley regions.

The raw data and associated metadata are publicly available through a published dataset on DesignSafe (Ornelas et al. 2023). Processed mHVSR mean curves and data are available through the VSPDB at https://vspdb.org/ (Kwak et al. 2021).

3.5 BORINGS

During May 22-23, 2023, four borings were hand augered to depths ranging from 2.2 to 4.0 m below the lakebed surface (Elevation of 497.1 m above sea level). One boring, HA-1R, was hand augered on the road grade (Elevation 498.5 m above sea level) approximately 7 m to the west of SCPT-1. The other three borings, HA-1, HA-3, and HA-4 were hand augered on the lakebed surface in areas where surface manifestation of liquefaction was observed by the reconnaissance team following the EQ sequence (Zimmaro et al 2020).

At boring HA-1, lacustrine clay was encountered to a depth of 1.68 m. Beneath that, silty sand was encountered with a blackish hue consistent with the liquefaction ejecta observed during the reconnaissance to a depth of 2.44 m at which point the boring was terminated. Figure 3.15 depicts the stratigraphy of HA-1.

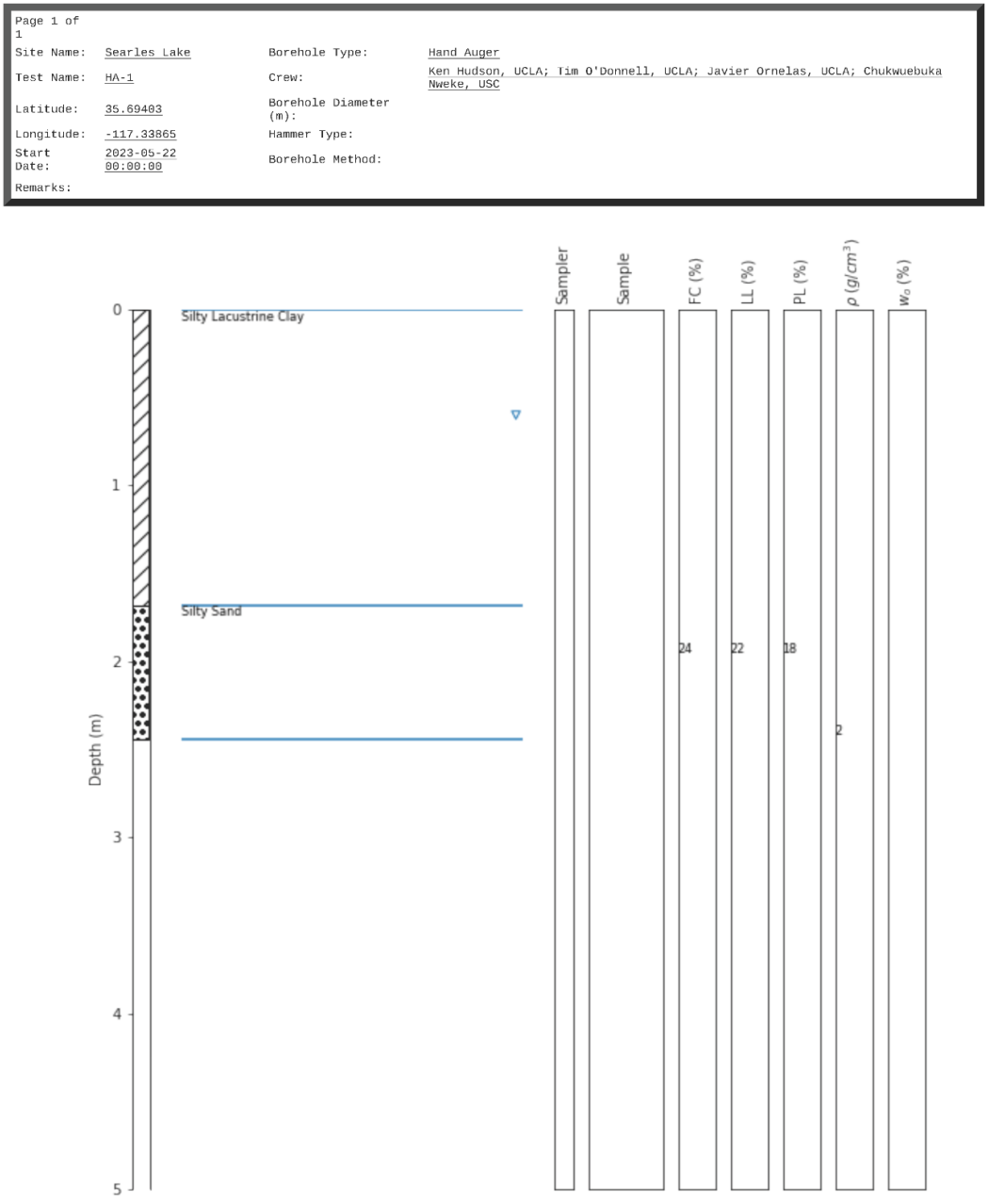

Figure 3.15. Boring log for HA-1.

At boring HA-1R, sandy and clayey embankment fill was encountered to a depth of 1.37 m. Beneath that, lacustrine clay was encountered to a depth of 3.2 m. Beneath the lacustrine clay, sand was encountered with a blackish hue consistent with the liquefaction ejecta observed during the reconnaissance to a depth of 3.35 m at which point the boring was terminated. Figure 3.16 depicts the stratigraphy of HA-1R.

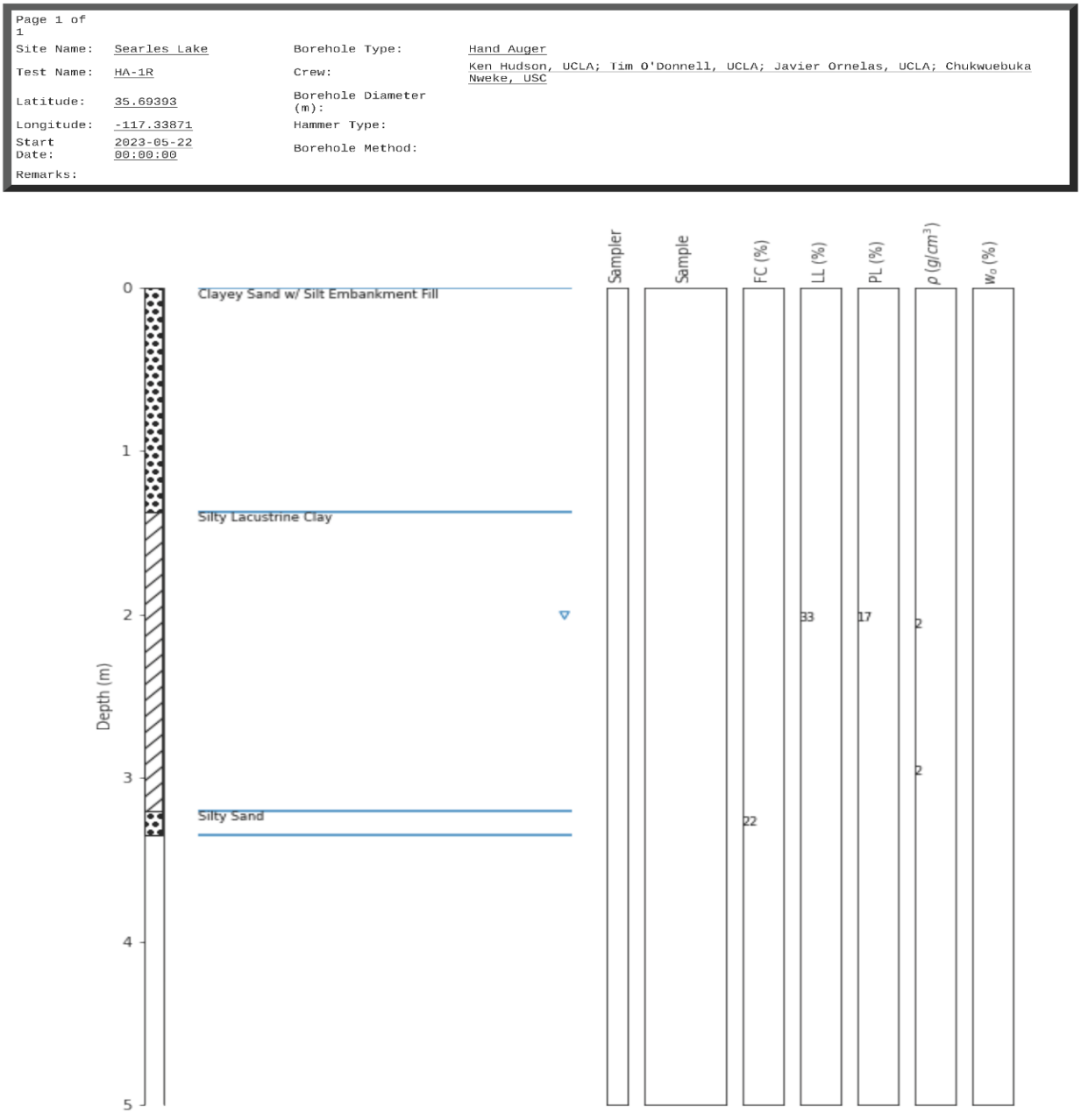

Figure 3.16. Boring log for HA-1R.

At boring HA-3, which was advanced in the free-field rather than through the embankment crest, lacustrine clay was encountered to a depth of 0.2 m followed by a thin layer of golden brown sand to a depth of 0.33 m. Then lacustrine clay was again encountered to a depth of 2.13 m where sand was encountered with a blackish hue, consistent with the liquefaction ejecta observed during the reconnaissance, to a depth of 3.12 m. Lacustrine clay was then encountered to a depth of 3.35 m where sand with a blackish hue was again encountered to a depth of 3.61 m at which point the boring was terminated. Figure 3.17 depicts the stratigraphy of HA-3.

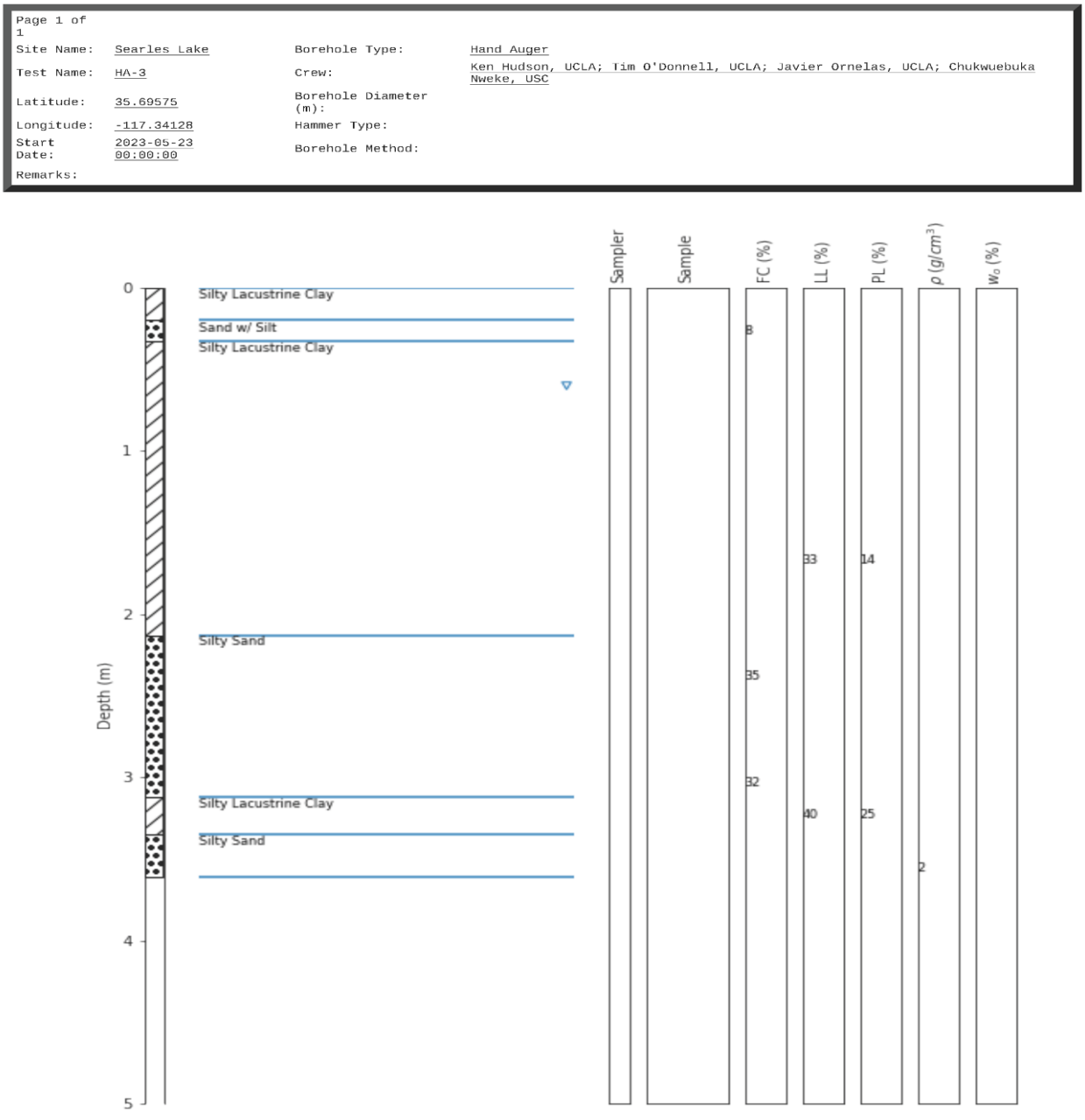

Figure 3.17. Boring log for HA-3.

At boring HA-4, also in the free-field, lacustrine clay was encountered to a depth of 0.66 m followed by a layer of black sand to a depth of 0.91 m. Then lacustrine clay was encountered to a depth of 3.2 m where black sand, consistent with the shade of the liquefaction ejecta documented after the earthquake sequence, was encountered to a depth of 3.96 m at which point the boring was terminated. Figure 3.18 depicts the stratigraphy of HA-4.

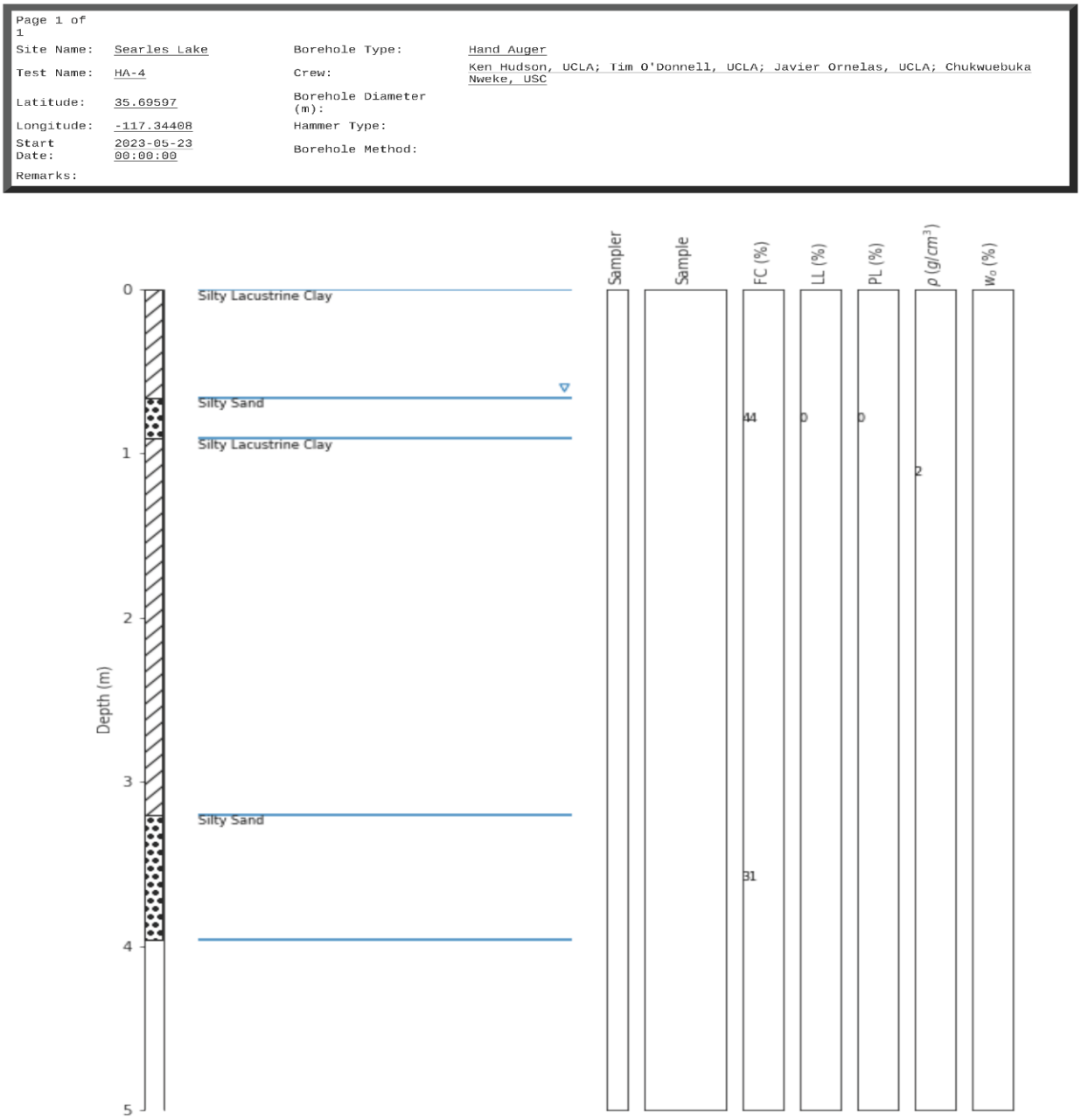

Figure 3.18. Boring log for HA-4.

3.6 WATER TABLE DETERMINATION

The water table depth of 0.6 m below the lakebed surface (and 2.0 m below the embankment surface), as depicted in the boring logs and CPT soundings, was estimated using a combination of methods. Pore pressure dissipation tests (not shown for brevity) were conducted during the CPT soundings, but were inconclusive, with different soil layers implying different groundwater elevations. In some cases, the dissipation tests had not stabilized when they were terminated, and it is unclear the extent to which the measured pore pressures deviated from steady-state pore

pressures. Furthermore, it is unclear whether groundwater is hydrostatic at this site due to mining operations in which pressurized heated fluids are used to dissolve the evaporites. We also utilized soil consistency encountered during hand auger operations to infer where soils transitioned from being unsaturated to saturated. This was inferred from soil consistency and color.

3.7 LABORATORY TESTING

A number of Shelby tube samples and disturbed samples were obtained from the hand augered borings at various depths to facilitate laboratory testing to better characterize the soil layers. Following subsurface exploration, the samples were transported to the UCLA research lab where the testing was performed between May and December of 2023. Table 3.4 summarizes the samples on which laboratory testing was performed.

Table 3.4. Samples obtained from site investigation for laboratory testing.

Sample Name	Boring	Sample Type	Sample Top (m)	Sample Bottom (m)	Laboratory Tests Performed			
					Specific Gravity	Bulk Density	Atterberg Limits	Grain Size Distribution
HA-1.1	HA-1	Disturbed	1.68	2.18	X		X	X
HA-1.2	HA-1	Shelby	2.18	2.43		X		
HA-1R.1	HA-1R	Shelby	1.83	2.08		X	X	
HA-1R.2	HA-1R	Shelby	2.74	2.99		X		
HA-1R.3	HA-1R	Disturbed	3.2	3.35	X			X
HA-3.1	HA-3	Disturbed	0.2	0.33	X			X
HA-3.2	HA-3	Shelby	1.47	1.72			X	
HA-3.3	HA-3	Disturbed	2.13	2.64	X			X
HA-3.4	HA-3	Disturbed	2.95	3.12	X			X
HA-3.5	HA-3	Disturbed	3.12	3.35			X	
HA-3.6	HA-3	Shelby	3.35	3.6		X		
HA-4.1	HA-4	Disturbed	0.66	0.91	X		X	X
HA-4.2	HA-4	Shelby	0.91	1.16		X		
HA-4.3	HA-4	Disturbed	3.2	3.96	X			X

3.7.1 Index Testing

To obtain unit weight characteristics of the soil to facilitate effective stress calculations, both specific gravity and bulk density tests were performed on specimens obtained from various samples.

Specific gravity tests were performed in accordance with ASTM D854-14 Method B on samples recovered from all of the encountered sand layers to measure the specific gravity of solids. The

values of specific gravity of solids obtained for all of the sand samples were between 2.66 and 2.74. These values are consistent with the industry standard of practice of assuming a value between 2.65 and 2.7 for the specific gravity of solids.

The bulk density was calculated for various Shelby tube samples by carefully extruding test specimens, cutting a 1-inch-long section of the soil with a wire saw, and weighing the specimen. This value can easily be converted to unit weight by dividing it by the specimen volume. These values are important for effective stress calculations which are necessary for interpreting the CPT data. The results for both the specific gravity and bulk density tests are presented in Table 3-5.

Table 3.5. Results of specific gravity and bulk density testing.

Sample Name	Boring	Sample Type	Sample Top (m)	Sample Bottom (m)	Specific Gravity	Bulk Density (g/cm^3)
HA-1.1	HA-1	Disturbed	1.68	2.18	2.66	
HA-1.2	HA-1	Shelby	2.18	2.43		2.03
HA-1R.1	HA-1R	Shelby	1.83	2.08		1.7
HA-1R.2	HA-1R	Shelby	2.74	2.99		1.63
HA-1R.3	HA-1R	Disturbed	3.2	3.35	2.66	
HA-3.1	HA-3	Disturbed	0.2	0.33	2.74	
HA-3.3	HA-3	Disturbed	2.13	2.64	2.66	
HA-3.4	HA-3	Disturbed	2.95	3.12	2.65	
HA-3.6	HA-3	Shelby	3.35	3.6		1.98
HA-4.1	HA-4	Disturbed	0.66	0.91	2.74	
HA-4.2	HA-4	Shelby	0.91	1.16		1.57
HA-4.3	HA-4	Disturbed	3.2	3.96	2.7	

3.7.2 Grain Size Distribution

Grain size distribution tests were performed in general accordance with ASTM D6913-04 on samples recovered from all of the encountered sand layers. The first step of testing consisted of washing test specimens through a No. 200 sieve (0.075 mm opening), oven drying the portion

retained by the No. 200 sieve, and allowing the portion passing the No. 200 sieve to settle to the bottom of the bucket used for wet sieving. After allowing the portion passing the No. 200 sieve to settle for approximately a week, the water on top of the settled soil was syphoned and the remaining soil was oven dried. Then the oven dried portions of the specimens that passed and that were retained on the No. 200 sieve were weighted.

It was after carrying out this process on samples HA-1.1, HA-1R.1, and HA-3.1 that it was discovered that a sizeable percentage of the fine portion of the original sample (between 17 and 27%) was going unaccounted for (the mass of the total oven dried sample was larger than the combined masses of the dried portion of the sample passing the No. 200 sieve and the dried portion of the sample retained on the number 200 sieve). We hypothesized that dissolved solids, such as sodium chloride and borax, might be responsible for this discrepancy. The mass of these constituents were going unaccounted for because they were being removed when the water was siphoned from the top of the soil.

For the remaining samples (HA-3.3, HA-3.4, HA-4.1, and HA-4.2), all of the siphoned water as part of the wet sieving process was placed into metal bowls and oven dried along with the fines settled at the bottom of the buckets. This process revealed the presence of a significant portion of dissolved solids in the siphoned water, as depicted in Figure 3.19.

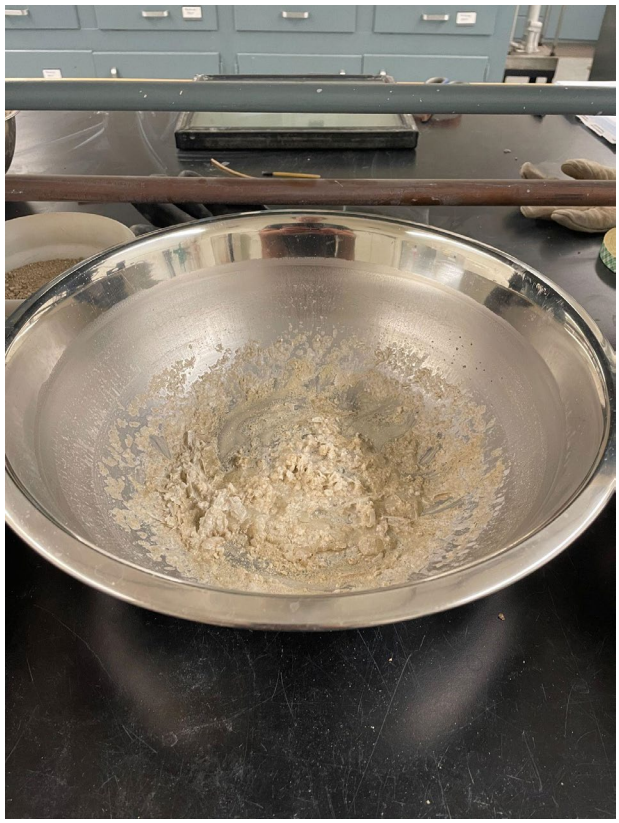

Figure 3.19. Metal bowl containing dissolved solids present after oven drying siphoned water from wet sieving.

For all of the specimens, the mass of the dissolved solids was calculated as follows:

$$m_{dissolved\ solids} = m_{total} - (m_{>\#200} + m_{<\#200}) \quad (3.9)$$

where $m_{dissolved\ solids}$ is the mass of dissolved solids, m_{total} is the total mass of the oven dried sample, $m_{>\#200}$ is the mass of the oven dried portion retained on the No. 200 sieve, and $m_{<\#200}$ is the mass of the oven dried portion of the sample passing the No. 200 sieve that had settled to the bottom of the bucket after wet sieving.

The ratio of dissolved solids to total mass (DS) was then calculated as follows:

$$DS\ (\%) = \frac{m_{dissolved\ solids}}{m_{total}} * 100\% \quad (3.10)$$

Results of these calculations are presented in Table 3-6. Most of the specimens had a dissolved solids ratio between 4.5 and 6.1 %, with HA-3.1 having a concentration of 2.6% and HA-4.2 having a concentration of 9.6%.

Table 3.6. Mass of dissolved solids gathered from samples.

Sample	m_{total} (g)	$m_{>\#200}$ (g)	$m_{<\#200}$ (g)	$m_{dissolved\ solids}$ (g)	DS (%)
HA-1.1	1649.3	1157	408	84	5.1
HA-1R.1	839.5	661	141	38	4.5
HA-3.1	274.1	248	19	7	2.6
HA-3.2	1114.5	751	308	56	5.0
HA-3.3	1801.3	1234	458	110	6.1
HA-4.1	1374.2	797	504	74	5.4
HA-4.2	1285.9	865	297	124	9.6

After quantifying the concentration of dissolved solids in each specimen, sieve analyses were performed on the portions of the specimens retained on the No. 200 sieve to obtain grain size distributions. Table 3.7 presents the sieves used for each analysis.

Table 3.7. Sieves used for sieve analyses.

Sieve No.	Sieve Opening (mm)
4	4.75
8	2.36
20	0.85
40	0.425
50	0.3
100	0.15
200	0.075

Figure 3.20 shows the grain size distributions obtained from the sieve analyses. As can be seen from Figure 3.20, the shapes of the gradation curves are very similar, being predominantly well graded between grain sizes of 0.5 and 0.1 mm. However, the grain size distribution of sample HA-3.1 is relatively distinct from the rest of the samples. This sample was recovered from a shallow sand lense that did not have the characteristic black hue of the layers that were ejected to the surface during the earthquake sequence.

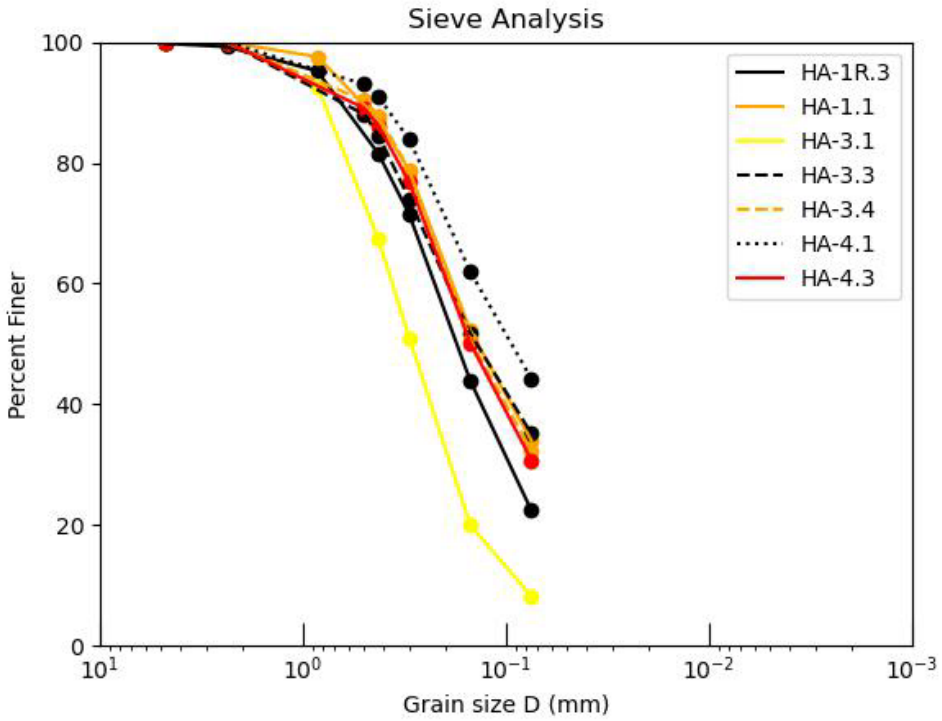

Figure 3.20. Grain size distributions of tested sand samples.

Table 3.8 summarizes the results of the grain size distribution most pertinent to classifying the soils with the Unified Soils Classification System (USCS). As can be seen, all specimens have greater than 12% fines with the exception of HA-3.1. The coefficient of uniformity (C_U) and the coefficient of curvature (C_C) calculated for HA-3.1 suggest that it is a poorly graded sand (USCS symbol SP). However, because it has a fines content greater than 5%, it requires a dual classification. The rest of the specimens have a fines content greater than 12%, therefore Atterberg Limits tests needed to be performed on the portion of the sample passing the No. 40 sieve (0.425 mm) in order to assign a final USCS classification.

Table 3.8. Parameters obtained from grain size distribution.

Sample	% Fines	Coefficient of Uniformity (C_U)	Coefficient of Curvature (C_C)
HA-1.1	34.0	3.14	0.56
HA-1R.1	22.4	2.48	0.40
HA-3.1	8.2	4.36	1.25
HA-3.2	35.1	2.71	0.37
HA-3.3	32.3	2.62	0.38
HA-4.1	44.2	1.89	0.53
HA-4.2	30.8	2.57	0.39

3.7.3 Atterberg Limits

In order to complete the USCS Classification of the sand samples discussed above, as well as selected samples of clay recovered from the site, the procedures outlined by ASTM D4318-17 (Liquid Limit Method A (Multipoint Method)) and ASTM D4318-17 (Plastic Limit Rolling Procedure 1 (Hand Rolling)) were performed to obtain liquid limits and plastic limits, respectively.

The first specimen tested was HA-1.1 utilizing only the portion of the sample passing the No. 40 sieve and fresh water. The resulting LL, PL, and PI were 22, 18, and 4, respectively. When plotted on Casagrande's plasticity chart, this resulted in a classification of CL-ML. This would normally result in a dual symbol of SC-SM. However, it was theorized that the significant dissolved solids concentration could have an effect on the sample's plasticity because cations are known to interact with the surface of clay minerals, thereby reducing their plasticity. Therefore, the next specimen that was tested was HA-4.1, the sand specimen with the highest fines content (44.2%). However, this time the test was run with water that had a dissolved solids concentration of 20% (similar to the measured dissolved solids concentration of the water of the samples). Using this pore fluid solution, the sample was non-plastic because a thread could not be rolled during the plastic limit

test, and the grooving tool could not cut a notch in the soil in the liquid limit test. Because this was the specimen with the highest fines content, it is safe to assume that the portion passing the No. 40 sieve of all of the sand specimen would classify as non-plastic, resulting in an overall classification for the sand samples of SM (silty sand).

To classify the clay located at representative depths throughout the site, Atterberg limits test were performed on specimens HA-1R.1, HA-3.2, and HA-3.5. These specimens were composed predominantly of clay by visual inspection, so they were not washed through a 200 sieve prior to the Atterberg limits test. As a result, any dissolved solids were still present in the specimens. The results of these tests are shown on Casagrande's plasticity chart in Figure 3.12 and tabulated in Table 3.9. All of the clay specimens were classified as low plasticity clay (USCS Symbol CL). Worksheets summarizing the Atterberg Limits test results are contained in the appendix.

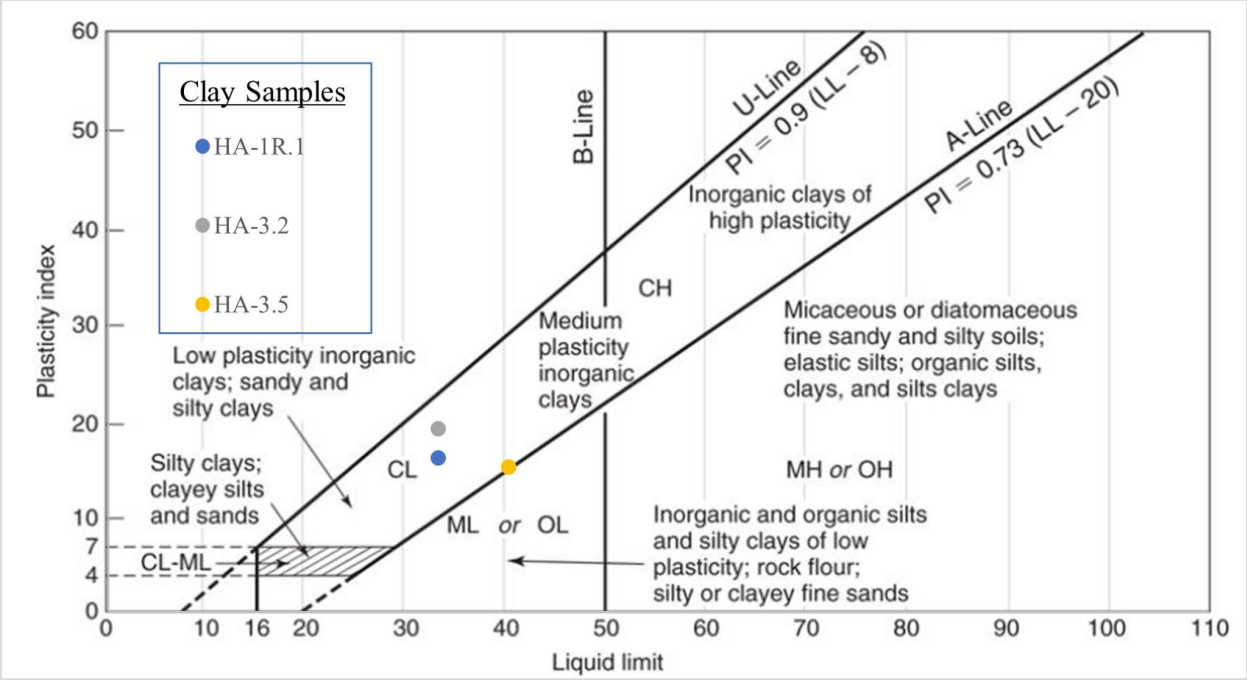

Figure 3.21. Atterberg limits results plotted on Casagrande's Plasticity Chart.

Table 3.9. Atterberg Limits test results.

Sample	Liquid Limit (LL)	Plastic Limit (PL)	Plasticity Index (PI)	USCS Classification
HA-1R.1	33	17	16	CL
HA-3.2	33	14	19	CL
HA-3.5	40	25	15	CL

3.8 SITE PROFILE

Based on the stratigraphies inferred through the CPTs and borings as well as the results of the laboratory tests, a site profile was developed for effective stress calculations which are necessary for processing the CPT data. The stratigraphic profile is based on the average depth to the respective layers based on SCPT-1, CPT-2, CPT-3, CPT-4, SCPT-6, HA-1, and HA-1R. Since the profile was to be used for the CPT data, the stratigraphies of HA-3 and HA-4 were not considered, as they are not in the general area of CPT soundings.

The unit weights of the upper lacustrine clay and both silty sand layers are based on the bulk density results. The embankment fill unit weight of 19 kN/m^3 was assumed as no sample of the embankment fill was collected. The unit weight of the middle and bottom lacustrine clay layers were assumed to be 17 and 18 kN/m^3 respectively to account for the tendency of soil to get denser and heavier with depth.

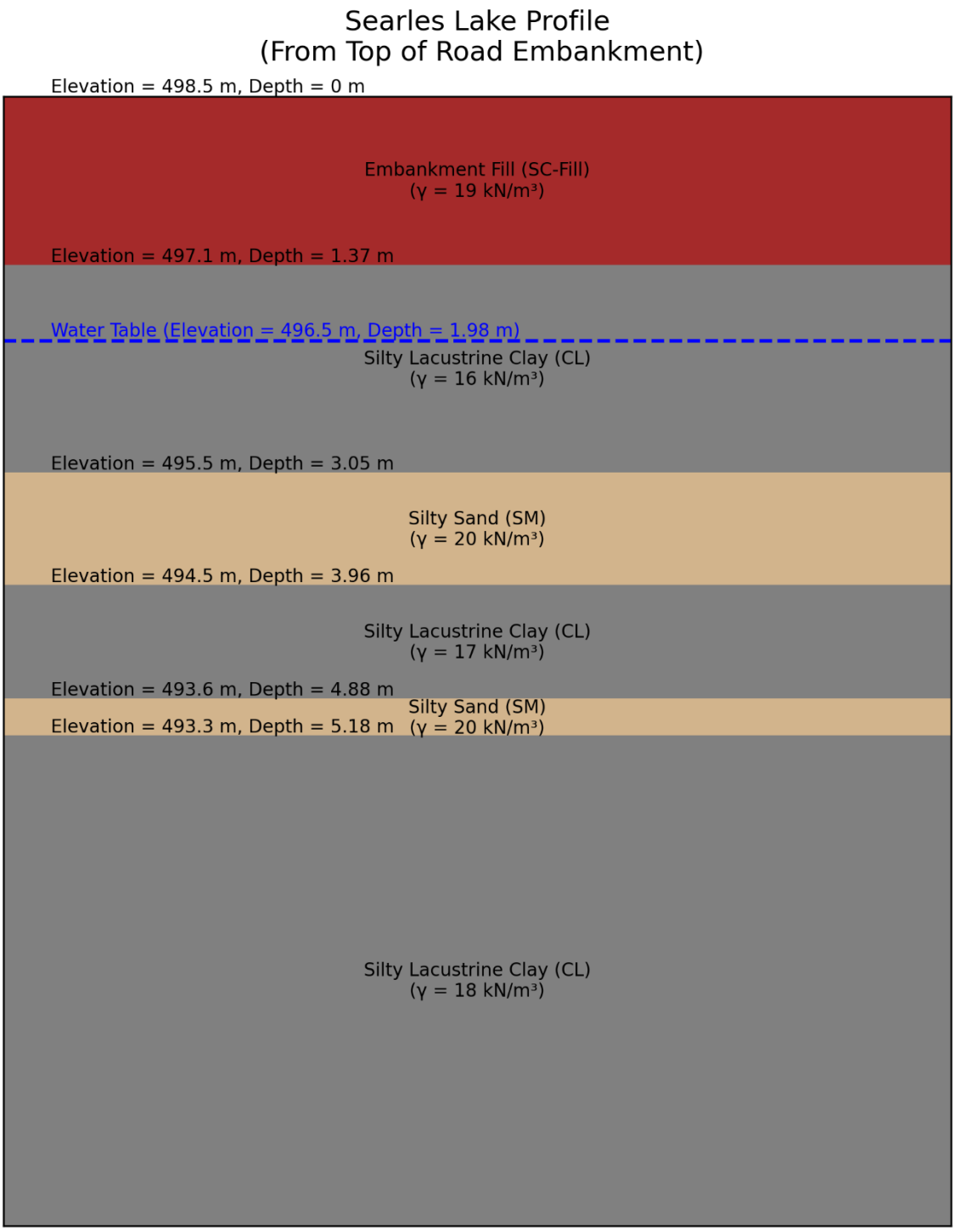

Figure 3.22. Site profile used for effective stress calculations.

4 LIQUEFACTION ANALYSIS

Using the data gathered from the site investigation, liquefaction triggering and manifestation analyses was performed using two different methods at each CPT location. The first method was the Boulanger and Idriss (2016) model, which is commonly considered to be a triggering model, but is in effect a model to predict manifestation of a triggered critical layer. The second method was the NGL supported modeling team (SMT) liquefaction model (Hudson 2023; Hudson et al. 2024), which was used to evaluate susceptibility and triggering of individual layers and the probability of liquefaction manifestation for the profiles.

4.1 PGA ESTIMATION WITH GMKRIGER

Liquefaction analyses for the CPT sites require estimation of Peak Ground Accelerations (PGA) for the two major events in the Ridgecrest Earthquake sequence. There were no ground motions recorded in the immediate vicinity of the testing sites (the nearest ground motion recording station was approximately 19 km away).

Ground motion intensity measures were estimated from regional recordings using an approach that spatially interpolates within-event residuals (Pretell et al. 2024). That approach accounts for local site response using the site V_{S30} (Table 3.3) with an ergodic model. The ground motion interpolation approach was implemented in the python program, gmKriger, which estimated the median-component Peak Ground Accelerations (PGAs) from the July 4 and July 5 events given in Table 4.1. These analyses used the coordinates of SCPT-1.

Table 4.1. PGA estimates from gmKriger.

Event	Latitude	Longitude	Vs30 (m/s)	PGA Estimate (g)	σ_{lnPGA}
M6.48	35.6939	-117.3386	175	0.234	0.509
M7.06	35.6939	-117.3386	175	0.280	0.477

Because the data and observed liquefaction manifestations could not be separated by event, the larger estimated PGA from the two events (PGA from the **M**7.06 event) was used for the liquefaction analyses.

4.2 EVALUATION USING BOULANGER AND IDRISS (2016) MODEL

The Boulanger and Idriss (2016) model requires evaluation of the critical layer for the purpose of assessing manifestation potential. The critical layers with respect to liquefaction were taken to be the shallowest layers below the groundwater table in each CPT that have a soil behavior index (I_c) less than 2.6, which is an established threshold for assessing liquefaction susceptibility (e.g.,

Maurer et al. 2017). We consider identification of the critical layer to be straightforward in this case. The mean q_{c1Ncs} was then computed, as summarized in Table 4.2.

Table 4.2. Critical layer data for each CPT.

CPT	Manifestation (Yes/No)	Top Depth (m)	Bottom Depth (m)	Median q_{c1Ncs}
SCPT-1	Yes	3.0	3.8	92
CPT-2	Yes	2.9	3.7	73
CPT-3	Yes	3.1	4.0	79
CPT-4	No	3.3	4.4	81
SCPT-6A	No	3.2	4.0	77

The cyclic stress ratio (CSR) for each critical layer was then estimated using Eq. 4.1, where σ_{vo} is the initial vertical total stress at the midpoint of the critical layer, σ'_{vo} is the initial vertical effective stress at the midpoint of the critical layer, and r_d is the stress reduction factor which was computed using the method by Boulanger and Idriss (2016).

$$\text{CSR} = 0.65 * \frac{PGA}{g} * \frac{\sigma_{vo}}{\sigma'_{vo}} * r_d \tag{4.1}$$

Additionally, a magnitude and overburden corrected cyclic stress ratio, $CSR_{M7.5,1atm}$, was computed using Eq. 4.2, where *MSF* is the magnitude scaling factor and K_σ is the overburden correction to account for the influence of contractiveness on liquefaction. MSF and K_σ were computed using equations in Boulanger and Idriss (2016).

$$CSR_{M7.5,1atm} = CSR \,/\, MSF \,/\, K_\sigma \tag{4.2}$$

The parameters necessary for the $CSR_{M7.5,1atm}$ calculation and the resulting $CSR_{M7.5,1atm}$ for each CPT are presented in Table 4.3.

Table 4.3. CSR calculations for each CPT.

CPT	Manifestation (Yes/No)	PGA (g)	σ_o (kPa)	σ'_{vo} (kPa)	r_d	MSF	K_σ	$CSR_{M7.5,1atm}$
SCPT-1	Yes	0.28	65	51	0.97	1.03	1.08	0.206
CPT-2	Yes	0.28	63	50	0.97	1.02	1.07	0.208
CPT-3	Yes	0.28	67	52	0.97	1.02	1.07	0.213
CPT-4	Yes	0.28	73	55	0.97	1.03	10.6	0.219
SCPT-6A	No	0.28	68	53	0.97	10.2	1.07	0.214

Values of $CSR_{M.7,1atm}$ and q_{c1Ncs} associated with each CPT are plotted along with the probabilities of liquefaction triggering developed by Boulanger and Idriss (2016), as depicted in Figure 4.1. The vertical and horizontal lines corresponding to each data point denote the one standard deviation ranges for $CSR_{M7.5,1atm}$ and q_{c1Ncs}, respectively, where the range for $CSR_{M7.5,1atm}$ was based on the

standard deviation of the interpolation error in the kriging analysis, and the range for q_{c1Ncs} was computed from the measured q_{c1Ncs} values over the depth range of the critical layer.

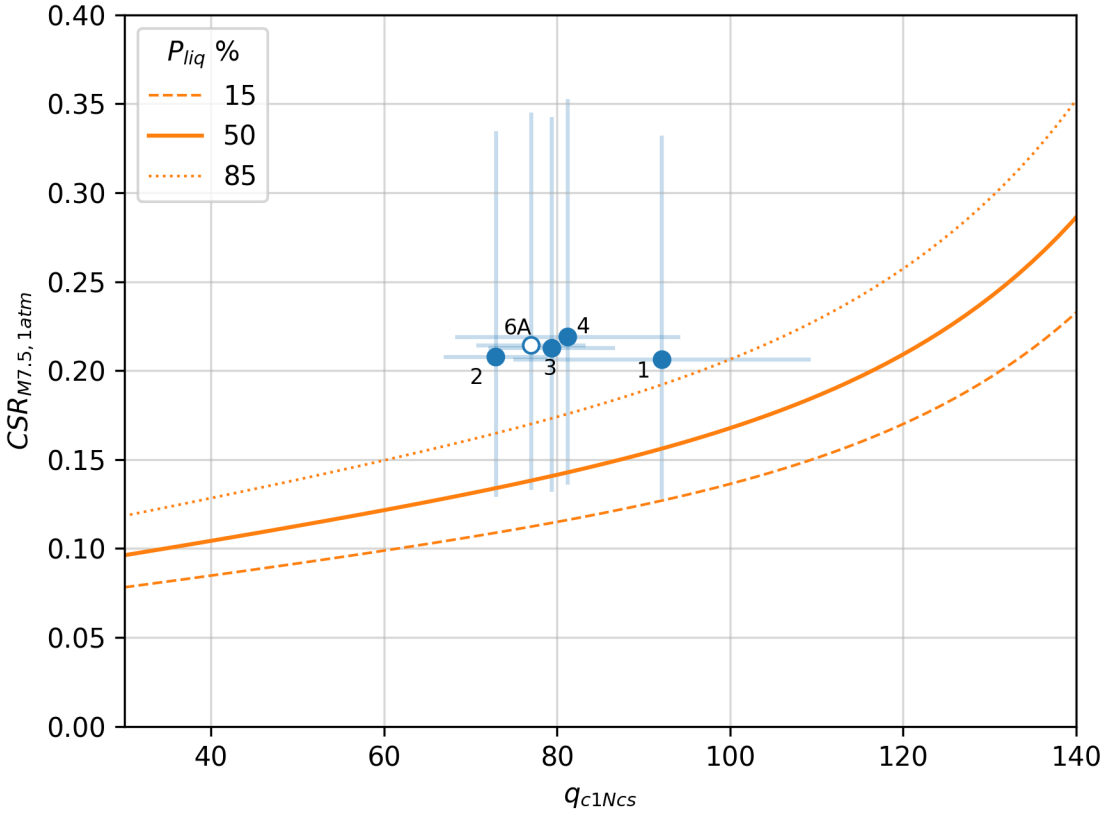

Figure 4.1. CSR vs. q_{c1Ncs} for the critical layer of each of the CPTs plotted against probabilities of liquefaction triggering developed by Boulanger and Idriss (2016). Numbers near the data points identify the corresponding CPT sounding.

The Boulanger and Idriss (2016) model predicts liquefaction at all of the CPT locations. Manifestations were observed at four of the five locations, so these are considered true positive predictions. Manifestations were not observed for CPT-6A, so this is a false positive prediction. Furthermore, the critical layer properties for CPT-6A are not significantly different from the other locations. The lack of manifestation at that location is therefore not well explained by differences in critical layer soil properties.

4.3 EVALUATION USING NGL SMT MODEL

A modeling team within the NGL project recently produced a new methodology for evaluating liquefaction susceptibility, triggering, and manifestation using a profile-based approach (Hudson

2023, Hudson et al. 2024). This model assesses the probability factor of susceptibility (PF_S), probability factor of triggering conditioned on susceptibility ($PF_{T|S}$), probability factor of triggering ($PF_T = PF_S \cdot PF_{T|S}$), probability factor of manifestation conditioned on triggering ($PF_{M|T}$), and the probability of manifestation (P[M_L]) for every layer within a CPT profile. Eqs. 4.1-4.6 express the models as a function of CPT variables, where K_{Sat} is a saturation factor, set to 0 for layers above the groundwater table and 1 for layers below the groundwater table, z_{top} is the depth to the top of the layer, t is the thickness of the layer, and t_c is the characteristic thickness, equal to 2m for this model.

$$PF_S = 1 - \frac{1}{1 + exp\left(\frac{-1.702 \cdot \left(\frac{I_c}{2.614} - 1\right)}{0.116}\right)} \tag{4.2}$$

$$C\hat{R}R = -7.427 + 0.0338 \cdot \left(\frac{\left(47.8 \cdot {q_{c1Ncs}}^{0.264} - 106.3\right)^{1.2022} - 1}{1.2022}\right) \tag{4.3}$$

$$C\hat{S}R = \frac{{CSR_{M7.5,1atm}}^{-0.6566} - 1}{-0.6566} \tag{4.4}$$

$$PF_{T|S} = \frac{1}{1 + exp\left(\frac{-1.702 \cdot \left(C\hat{S}R - C\hat{R}R\right)}{0.985}\right)} \cdot K_{Sat} \tag{4.5}$$

$$PF_{M|T} = \frac{1}{1 + exp\left(-\left(8.206 - 0.342 \cdot z_{top} - 3.461 \cdot I_c\right)\right)} \tag{4.6}$$

I_c is computed using a procedure given by Robertson (1990), q_{c1Ncs} is computed using the fines content (FC) correlation from Hudson et al. (2024) and the clean sand and stress corrections from Boulanger and Idriss (2014), and $CSR_{M7.5,1atm}$ is computed using the MSF from Green et al. (2016) with the number of equivalent cycles (N_{eq}) from Lasley et al. (2017) and r_d from Lasely et al. (2016).

To compute the P[M_L], the CPT profiles are first inverse-filtered using the method by Boulanger and DeJong (2018), and discretized into layers using the agglomerative clustering algorithm presented in Hudson et al. (2023). The median q_{c1Ncs}, I_c, and $CSR_{M7.5,1atm}$ within the depth range of each layer is taken as the representative value for that layer, and the depth to the top of each layer and thickness of each layer are taken as z_{top} and t, respectively.

The P[M_L] of each layer is aggregated using the complement of the product sum of the probability of no manifestation of a layer (P[NM_L] = 1 - P[M_L]) (Eq. 4.7) to compute the probability of manifestation of the profile, P[M_P], where N_L is the number of layers in the profile.

$$P[M_P] = 1 - \prod_{i=1}^{N_L} (1 - P[M_L]) \tag{4.7}$$

Using the site profile defined in Section 3.8, these probabilities are computed using the tip resistance and sleeve friction data from the five CPT soundings presented in Section 3.2. Figures 4.2 through 4.6 present the results of the probability factor calculations and Table 4.4 presents the P[M_P] predicted for each CPT sounding.

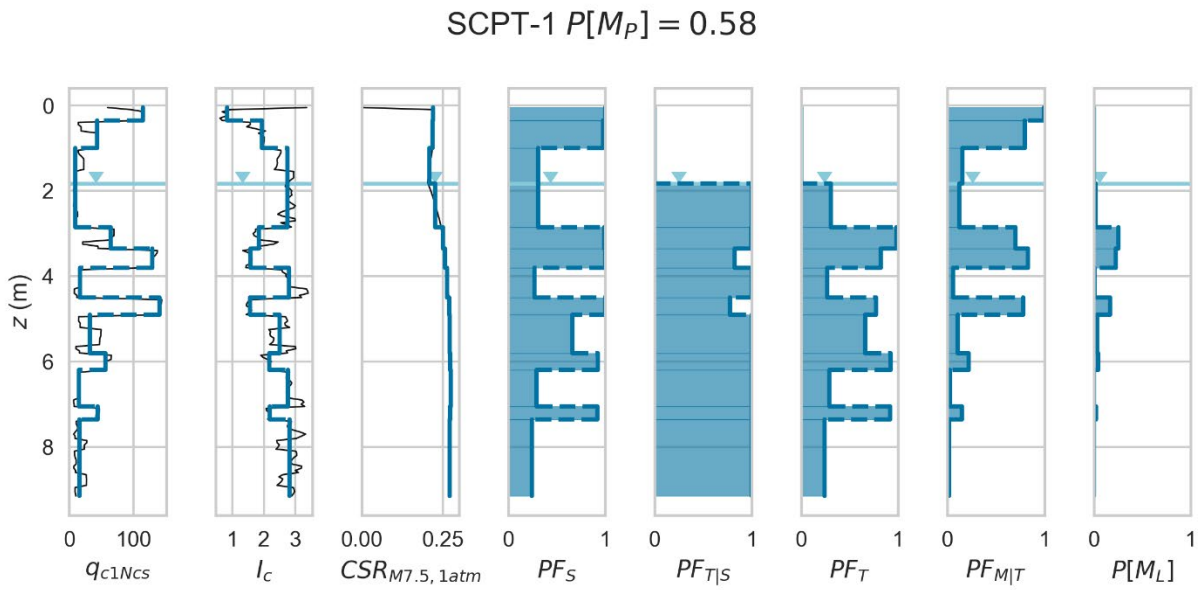

Figure 4.2. SCPT-1 sounding data, estimated $CSR_{M7.5,1atm}$, probability factors, and probability of manifestation of each layer. The q_{c1Ncs}, I_c, and $CSR_{M7.5,1atm}$ plots show the point-by-point data as a black line and the layered data as blue lines.

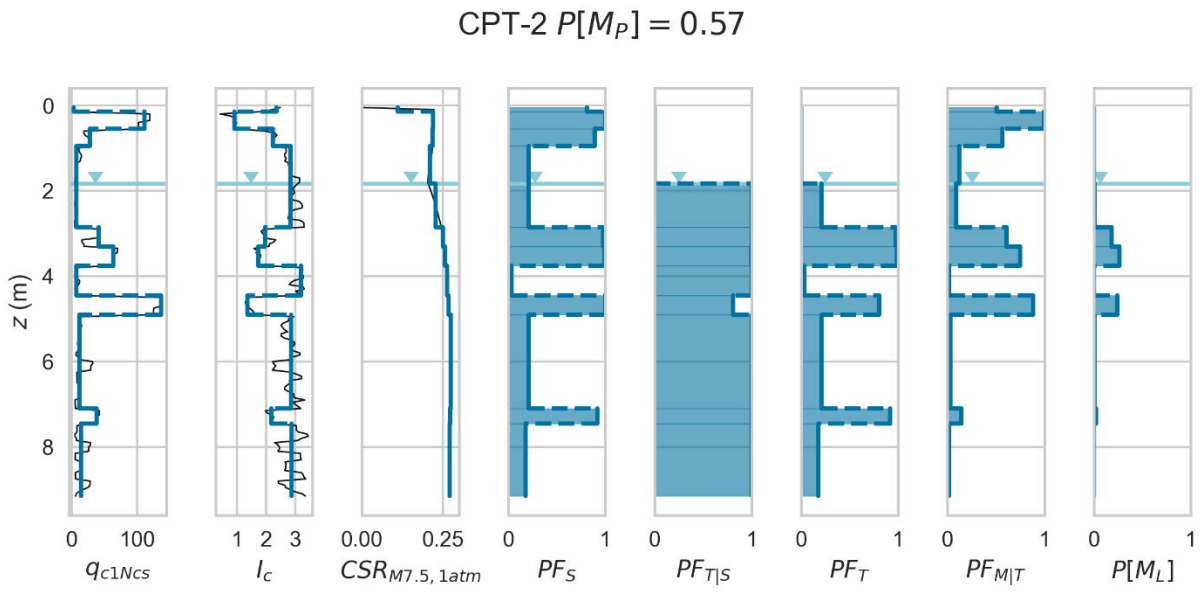

Figure 4.3. CPT-2 sounding data, estimated $CSR_{M7.5,1atm}$, probability factors, and probability of manifestation of each layer. The q_{c1Ncs}, I_c, and $CSR_{M7.5,1atm}$ plots show the point-by-point data as a black line and the layered data as blue lines.

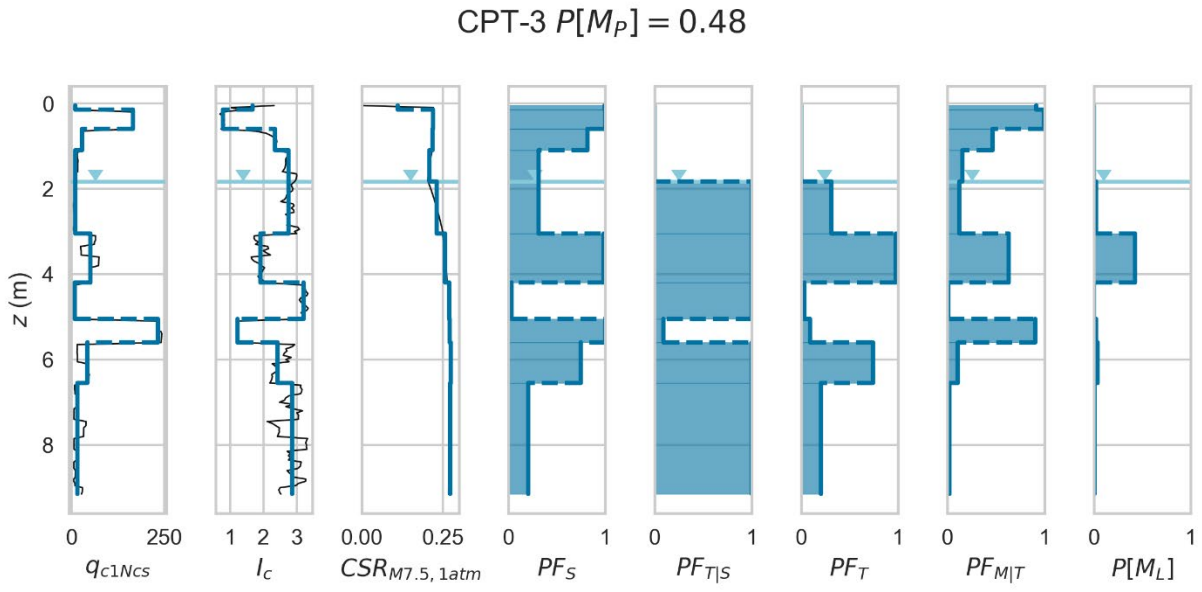

Figure 4.4. CPT-3 sounding data, estimated $CSR_{M7.5,1atm}$, probability factors, and probability of manifestation of each layer. The q_{c1Ncs}, I_c, and $CSR_{M7.5,1atm}$ plots show the point-by-point data as a black line and the layered data as blue lines.

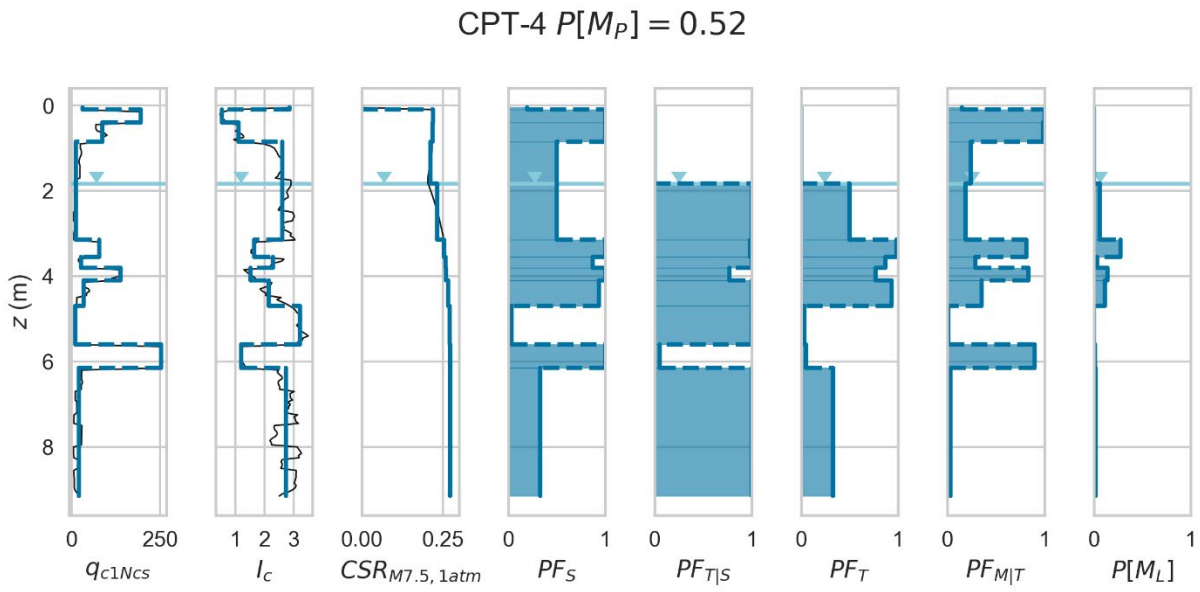

Figure 4.5. CPT-4 sounding data, estimated $CSR_{M7.5,1atm}$, probability factors, and probability of manifestation of each layer. The q_{c1Ncs}, I_c, and $CSR_{M7.5,1atm}$ plots show the point-by-point data as a black line and the layered data as blue lines.

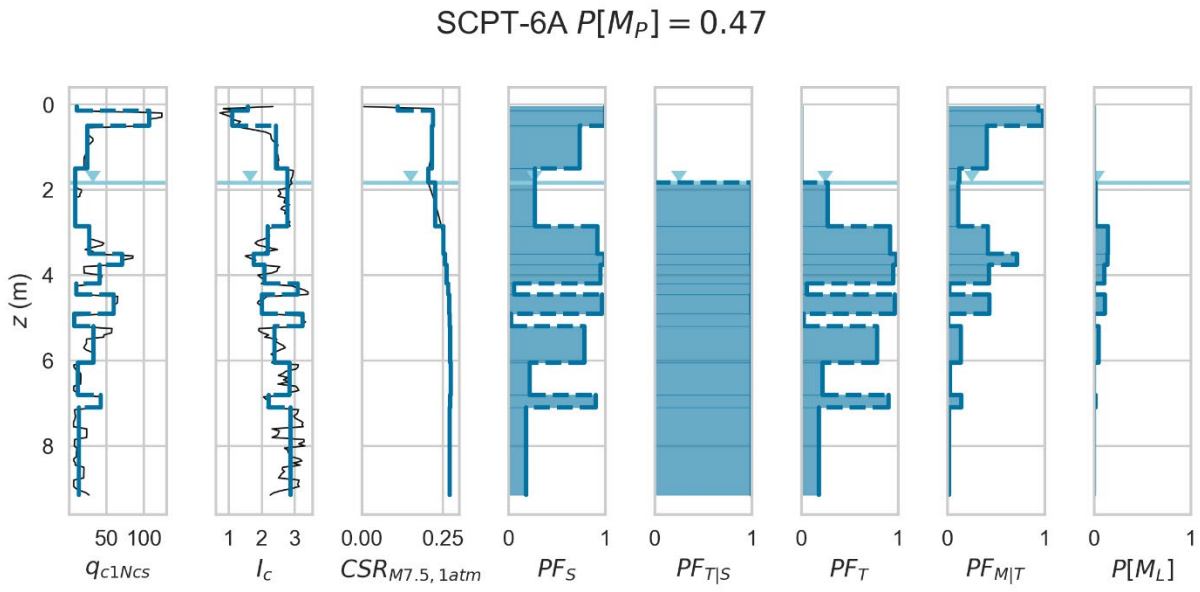

Figure 4.6. SCPT-6A sounding data, estimated $CSR_{M7.5,1atm}$, probability factors, and probability of manifestation of each layer. The q_{c1Ncs}, I_c, and $CSR_{M7.5,1atm}$ plots show the point-by-point data as a black line and the layered data as blue lines.

Table 4.4. Probability of profile manifestation (P[M_P]) predictions for the five CPT soundings obtained during the field investigation.

Test Name	P[MP]
SCPT-1	0.58
CPT-2	0.57
CPT-3	0.48
CPT-4	0.52
SCPT-6A	0.47

The high $CSR_{M7.5,1atm}$ and low q_{c1Ncs} at each profile causes $PF_{T|S}$ to be almost 1 for most layers. Triggering is suppressed in many layers because of the low PF_S (due to high I_c, and corresponding low susceptibility). There are a few layers that have both a high PF_T and $PF_{M|T}$, leading to significant P[M_L] values; these layers correspond with the silty sand layers described in the site profile. The shallower of the two silty sand layers, which was identified as the critical layer in the liquefaction analysis in the previous section, contributes more manifestation potential than the deeper sandy layer. This is because deeper liquefied layers are less likely to manifest at the surface.

Overall, the probability of manifestation of the profiles ranges from a high of 0.58 for SCPT-1 to a low of 0.47 for CPT-6A. There is little difference in the computed P[M_P] values, though they do span the threshold distinguishing a positive from a negative prediction. A positive prediction is considered to correspond to P[M_P] > 0.5, such that positive predictions are made for SCPT-1, CPT-2, and CPT-4, and negative predictions are made for CPT-3 and SCPT-6A. Therefore, SCPT-1, CPT-2, and CPT-4 are considered true positives, SCPT-6A is considered a true negative, and CPT-3 is considered a false negative. However, the strength of these true positives and true negatives is relatively weak since they are all close to 0.5.

5 SUMMARY AND CONCLUSIONS

This report presents a site investigation to characterize the subsurface of several locations in Searles Lake in an area where extensive surface manifestations of liquefaction were documented following the 2019 Ridgecrest Earthquake Sequence. Hand augered borings, cone penetration tests (CPTs), seismic cone penetration tests (SCPTs), and horizontal to vertical spectral ratio (HVSR) testing was conducted as part of this effort as well as additional laboratory testing on samples recovered from the hand augered borings including specific gravity, bulk density, grain size distribution, and Atterberg limits tests. Significantly, silty sand with a dark hue consistent with the color of sand boil ejecta documented after the 2019 Ridgecrest Earthquake Sequence was identified in the hand augered borings at depths ranging from approximately 1.5 to 4 m beneath the lakebed surface (0.9 to 3.4 m beneath the water table). The CPTs revealed material with a soil behavior index, I_c, of less than 2.6 in the same depth range. This evidence leads to the conclusion that this was the critical layer that experienced liquefaction during the 2019 Ridgecrest Earthquake sequence.

The data gathered from the site investigation was analyzed using two probability of liquefaction manifestation models: the critical layer-based liquefaction triggering and manifestation proposed by Boulanger and Idriss (2016) and the profile-based probability of liquefaction manifestation model developed as part of the next generation liquefaction supported modeling Team (NGL-SMT; Hudson et al. 2024). Using the median PGA estimate for the larger July 5 event, the Boulanger and Idriss (2016) model estimates a probability of critical layer liquefaction triggering and manifestation greater than 85% at all CPT locations, producing four true positive and one false positive prediction. The NGL model estimates a probability of liquefaction manifestation ranging from 47% to 58%, producing three true positives, one true negative, and one false negative prediction. However, these predictions were all close to the threshold.

REFERENCES

ASTM Standard D854-14. (2019). "Standard Test Methods for Specific Gravity of Soil Solids by Water Pycnometer", ASTM International, West Conshohocken, PA, 2019

ASTM Standard D4318-17. (2018). "Standard Test Methods for Liquid Limit, Plastic Limit, and Plasticity Index of Soils", ASTM International, West Conshohocken, PA, 2019

ASTM Standard D6913-04. (2009). "Standard Test Methods for Particle-Size Distribution (Gradation) of Soils Using Sieve Analysis", ASTM International, West Conshohocken, PA, 2009

Bonilla L. F., J. H. Steidl, J.-C. Gariel, and R. J. Archuleta. (2002). Borehole response studies at the Garner Valley downhole array, Southern California, *Bull. Seismol. Soc. Am.* **92**, 3165–3179.

Boulanger, R. W., and DeJong, J. T. (2018). "Inverse filtering procedure to correct cone penetration data for thin-layer and transition effects." Proc., Cone Penetration Testing 2018, Hicks, Pisano, and Peuchen, eds., Delft University of Technology, The Netherlands, 25-44.

Boulanger R. W., and I. M. Idriss. (2014). CPT and SPT based liquefaction triggering procedures. **259**. Davis, California: University of California, Davis.

Boulanger R. W., and I. M. Idriss. (2016). CPT-based liquefaction triggering procedure. *J. Geotech. Geoenviron. Eng.,* **142(2)**, 04015065.

Brandenberg S. J., C. A. Goulet, P. Wang, C. C. Nweke, C. A. Davis, M. B. Hudson, K. S. Hudson, S. K. Ahdi, and J. P. Stewart (2019). GEER field reconnaissance, in Ridgecrest, CA earthquake sequence, July 4 and 5, 2019, DesignSafe-CI, doi: 10.17603/ds2-vpmv-5b34.

Brandenberg S. J., J. P. Stewart, P. Wang, C. C. Nweke, K. S. Hudson, C. A. Goulet, X. Meng, C. A. Davis, S. K. Ahdi, M. B. Hudson, et al. (2020). Ground deformation data from GEER investigations of Ridgecrest earthquake sequence, *Seismol. Res. Lett.* **91, 2024-2034** doi: 10.1785/ 0220190291.

Buckreis T.E., Stewart, J.P., Brandenberg, S.J., and Wang, P. (2024). Small-strain site response of soft soils in the Sacramento-San Joaquin Delta region of California conditioned on VS30 and mHVSR, *Earthquake Spectra*, DOI: 10.1177/87552930231217165/

California DWR (2020). Water Data Library, available at http://wdl .water.ca.gov/waterdatalibrary/

Dai Z., X. Li, and C. Hou (2013). A shear-wave velocity model for *VS*30 estimation based on a conditional independence property, *Bull. Seism. Soc. Am.*, **103**, 3354–3361.

DuRoss C. B., R. D. Gold, T. E. Dawson, K. M. Scharer, K. J. Kendrick, S. O. Akciz, S. J. Angster, J. Bachhuber, S. Bacon, S. E. K. Bennett, et al. (2020). Surface displacement distributions for the July 2019 Ridgecrest, California, earthquake ruptures, *Bull. Seismol. Soc. Am.*, **110**: 1400–1418.

Frankel K. L., A. F. Glazner, E. Kirby, F. C. Monastero, M. D. Strane, M. E. Oskin, J. Unruh, J. Walker, S. Anandakrishnan, J. M. Bartley, D. S. Coleman, J. F. Dolan, R. Finkel, D. Greene, A. Kylander-Clark, S. Marrero, L. A. Owen, and F. Phillips (2008). Active Tectonics of the Eastern California Shear Zone. In Frankel, K. L., & Glazner, A. F. (Eds.), *GSA Field Guide 11: Field Guide to Plutons, Volcanoes, Faults, Reefs, Dinosaurs, and Possible Glaciation in Selected Areas of Arizona, California, and Nevada*, (, pp. 43-81) Boulder, : *Geological Society of America* doi: 10.1130/2008.fld011(03).

Green R., J. Bommer, A. Rodriguez-Marek, and P. Stafford. (2016). Unbiased Cyclic Resistance Ratio Relationships for Evaluating Liquefaction Potential in Groningen. 61. Virginia, USA: NAM.

Hudson K. S., K. J. Ulmer, P. Zimmaro, S. L. Kramer, J. P. Stewart, and S. J. Brandenberg. (2023). "Unsupervised machine learning for detecting soil layer boundaries from cone penetration test data." *Earthq Engng Struct Dyn*, **52** (11): 3201–3215.

Hudson K. S. (2023). "Next Generation Liquefaction Database and Probabilistic Liquefaction Model Development." ProQuest Dissertations and Theses. Ph.D. United States -- California: University of California, Los Angeles.

Hudson K. S., K. Ulmer, S. J. Brandenberg, P. Zimmaro, S. L. Kramer, and J. P. Stewart. (2024). "A Framework for Probabilistic Assessment of Liquefaction Manifestation." *Geo-Congress 2024: Geotechnics of Natural Hazards*, **152–160**. Vancouver, British Columbia, Canada: American Society of Civil Engineers.

Hudson K. S., K. J. Ulmer, P. Zimmaro, S. L. Kramer, J. P. Stewart, and S. J. Brandenberg. (2024). "Relationship between Fines Content and Soil Behavior Type Index at Liquefaction Sites." *J. Geotech. Geoenviron. Eng.*, **150** (5): 06024001.

Kawase H., F. J. Sánchez-Sesma, and S. Matsushima (2011). The optimal use of horizontal-to-vertical spectral ratios of earthquake motions for velocity inversions based on diffuse-field theory for plane waves, *Bull. Seismol. Soc*. Am. **101**, 2001–2014.

Kunkel, F., and G. H. Chase (1969). Geology and ground water in Indian Wells Valley, California, U.S. Geol. Surv. Open-File Rept., 84 pp.

Kwak, D. Y., S. K. Ahdi, P. Wang, P. Zimmaro, S. J. Brandenberg, and J. P. Stewart (2021). Web portal for shear wave velocity and HVSR databases in support of site response research and applications. UCLA Geotechnical Engineering Group. DOI:10.21222/C27H0V

Lachet, D., C. Hatzfeld, P.-Y. Bard, N. Theodulis, C. Papaioannou, and A. Savvaidis (1996). Site effects and microzonation in the city of Thessaloniki (Greece): Comparison of different approaches, *Bull. Seismol. Soc. Am.* **86**, 1692–1703.

Lasley, S. J., R. A. Green, and A. Rodriguez-Marek. (2016). "New Stress Reduction Coefficient Relationship for Liquefaction Triggering Analyses." *J. Geotech. Geoenviron. Eng*., **142** (11): 06016013.

Lasley, S. J., R. A. Green, and A. Rodriguez-Marek. (2017). "Number of Equivalent Stress Cycles for Liquefaction Evaluations in Active Tectonic and Stable Continental Regimes." *J. Geotech. Geoenviron. Eng.*, **143** (4): 04016116. https://doi.org/10.1061/(ASCE)GT.1943-5606.0001629

Lermo, J., and F. J. Chávez-García (1993). Site effect evaluation using spectral ratios with only one station, *Bull. Seismol. Soc. Am.* **83**, 1574–1594.

Liu M., H. Wang H, and Q. Li (2010). Inception of the eastern California shear zone and evolution of the Pacific-North American plate boundary: From kinematics to geodynamics. *Journal of Geophysical Research.* Volume **115**, Issue B7

Mauer, B. W., R. A. Green, S. V. Ballegooy, and L. Wotherspoon (2017) Assessing Liquefaction Susceptibility using the CPT Soil Behavior Type Index. PBD Vancouver Earthquake Geotechnical Engineering.

McGraw, D., R. Carroll, G. Pohll, J. Chapman, S. Bacon, and R. Jasoni (2016). Groundwater resource sustainability: Modeling evaluation for the Naval Air Weapons Station, China Lake, Desert Research Institute for Naval Air Warfare Center Weapons Division, China Lake, California, NAWCWD Technical Publication 8811, available at https://apps.dtic.mil/dtic/tr/fulltext/u2/1070491.pdf.

Nakamura, Y. (1989). A method for dynamic characteristics estimation of subsurface using microtremors on the ground surface, Quarterly Report of Railway Technical Research Institute (RTRI), **30**, 25-33.

Nogoshi, M., and T. Igarashi (1971). On the amplitude characteristics of microtremor (part 2*). Journal of Seismological Society of Japan* **24**, 26–40 (In Japanese with English abstract).

Ornelas, F.G., C.C. Nweke, C.A. de la Torre, P. Wang, T.D. Mai, B.R. Cox, S.J. Brandenberg, and J.P. Stewart. (2024b). Reliability of Low Frequency mHVSR Ordinates. *18th World Conference on Earthquake Engineering Conference*. Italy. submitted.

Ornelas, F., C. Nweke, T. O'Donnell, K. Hudson, S. Brandenberg, J. Stewart, (2023) Microtremor Horizontal-to-Vertical Spectral Ratio (mHVSR) Data Collection at Searles Lake, 2023, in *Microtremor Horizontal-to-Vertical Spectral Ratio (mHVSR) Site Characterization of California Vertical Arrays*. DesignSafe-CI. https://doi.org/10.17603/ds2-1fcj-p013 v2

Ponti, D. J., J. L. Blair, C. M. Rosa, K. Thomas, A. J. Pickering, S. Akciz, S. Angster, J.-P. Avouac, J. Bachhuber, S. Bacon, et al. (2020). Documentation of surface fault rupture and ground deformation features produced by the Ridgecrest M 6.4 and M 7.1 earthquake sequence of July 4 and 5, 2019, *Seismol. Res. Lett*. **91**, 2942–2959.

Pretell, R., S.J. Brandenberg, J.P. Stewart. "Ground motion intensity measures at liquefaction field case history sites." Report GIRS-2024-02, B. John Garrick Risk Institute, Natural Hazards Risk and Resiliency Research Center, UCLA (Center Headquarters), 2024.

Pretell, R. (2024). gmKriger: A Kriging-based ground motion intensity measure calculator (0.2.0). Zenodo. https://doi.org/10.5281/zenodo.10691892

Schweig, E. S., III (1984). Neogene tectonics and paleogeography of the southwestern Great Basin, Inyo County, California: Palo Alto, California, Ph.D. Dissertation, Stanford University, Stanford, California, 207 pp.

Smith, G. I. (1979). Subsurface stratigraphy and geochemistry of late Quaternary evaporites, Searles Lake, California, U.S. Geol. Surv. Profess. Pap. 1043, 130 pp.

Smith, G. I. (2009). Late Cenozoic Geology and Lacustrine History of Searles Valley, Inyo and San Bernardino Counties, California, U.S. Geol. Surv. Profess. Pap. 1727, 115 pp., 4 plates.

Stewart J. P., S. L. Kramer, D. Y. Kwak, M. W. Greenfield, R. E. Kayen, K. Tokimatsu, J. D. Bray, C. Z. Beyzaei, M. Cubrinovski, T. Sekiguchi, S. Nakai, and Y. Bozorgnia (2016). PEER-NGL project: Open source global database and model development for the next-generation of liquefaction assessment procedures, *Soil Dynamics and Earthquake Engineering* **91**, 317-328.

Theodulidis, N., R. J. Archuleta, P.-Y. Bard, and M. Bouchon (1996). Horizontal to vertical spectral ratio and geological conditions: The case of Garner Valley downhole array in southern California, Bull. *Seismol. Soc. Am*. **86**, 306–319.

Ulmer, K. J., R. A. Green, A. Rodriguez-Marek (2020). A Consistent Correlation Between Vs, SPT, and CPT Metrics for Use in Liquefaction Evaluation Procedures. *Geo-Congress 2020*

Wair, B. R., J. T. DeJong, and T. Shantz (2012). *Guidelines for estimation of shear wave velocity profiles.* PEER Report 2012/08, Pacific Earthquake Engineering Research Center, Berkeley, CA.

Wang, P. (2021). wltcwpf/hvsrProc: First release (v1.0.0), Zenodo, doi:10.5281/zenodo.4724141.

Wang, P., Y. T. Tsai, J. P. Stewart, A. Mikami, and S. J. Brandenberg, S. J. (2022a): Region-specific linear site amplification model for peaty organic soil sites in Hokkaido, *Japan. Earthquake Spectra* **38**, 2207-2234.

Wang, P., P. Zimmaro, T. E. Buckreis, T. Gospe, S. J. Brandenberg, S. K. Ahdi, A. Yong, and J. P. Stewart (2022b). Relational Database for Horizontal-to-Vertical Spectral Ratios, *Seismol. Res. Lett.* **93**, 1075–1088, doi: 10.1785/0220210128.

Zimmaro, P., and K. Hudson (2019). Searles lake liquefaction, in Ridgecrest, CA earthquake sequence, July 4 and 5, 2019, DesignSafe-CI, doi: 10.17603/ds2-9wp5-rp81.

Zimmaro P., C. C. Nweke, J. L. Hernandez, K. S. Hudson, M. B. Hudson, S. K. Ahdi, M. L. Boggs, C. A. Davis, C. A. Goulet, S. J. Brandenberg, K. W. Hudnut, J. P. Stewart (2020). *Bulletin of the Seismological Society of America,* **110**, 1549-1566.